Geochemistry and mineralogy of a saprolite developed on Columbia River Basalt: Secondary clay formation, element leaching, and mass balance during weathering

(Revision 3)

Leslie L. Baker
Department of Geological Sciences
University of Idaho
875 Perimeter Drive MS 3022
Moscow, ID 83844
lbaker@uidaho.edu

and

Owen Kelly Neill
Peter Hooper GeoAnalytical Lab
School of the Environment
Washington State University
P.O. Box 642812
Pullman, WA 99164-2812
owen.neill@wsu.edu

Abstract

This study presents chemical and mineralogical data on weathering trends in a saprolite that is preserved between flows of the Columbia River Basalt Group at Trinidad, WA. Bulk chemistry, electron imaging, and X-ray mapping indicate early Fe and Mg depletion by dissolution of ferromagnesian minerals, followed by depletion of alkalis, Al, Ti, and P, corresponding to dissolution of feldspars, titanomagnetite, and apatite. Secondary coatings of nontronite clay in the deep saprolite display intricate, sub-micron scale zoning in Fe and Mg content. Distinct aluminous zones in these clays become more prominent at shallower depths. The primary Fe-containing phase shifts from nontronite in deeper samples to hematite in shallow samples; samples at the boundary contain the assemblage kaolinite + nontronite, which may mark the transition from permeability-limited fluid flow to fully open-system behavior. This shift is observed in rocks that have lost 30-40% of the total rock mass to leaching, and coincides with the disappearance of feldspar, Fe-Ti oxides, and apatite. Rocks in the uppermost saprolite have been converted to an assemblage of Al-smectite + hematite (+kaolinite). These results suggest that the presence of nontronite in weathered samples may indicate weathering under conditions of limited permeability; however, it does not necessarily indicate weathering in a chemically closed system. These observations may be useful in interpreting the clay mineral assemblages observed on Mars and what information they contain about near-surface conditions in the planet's ancient past.

Introduction

The weathering of fresh volcanic rocks, and particularly of fresh basaltic rock, is a major factor controlling ocean chemistry, atmospheric CO_2 fixation, and ultimately, terrestrial climate (Gaillardet et al. 1999; Kump et al. 2000; Benedetti et al. 2003; Dessert et al. 2003; Dupré et al. 2003; Gislason et al. 2009; Maher and Chamberlain 2014). These studies indicate that weathering of basaltic lavas is responsible for approximately one third of global CO_2 fixation by weathering of continental rocks, with much of this accounted for by weathering of young basalts in warm, wet tropical localities. Subsurface weathering of volcanic rocks can be, quantitatively, an even more significant ion source and carbon sink than surface weathering (Rad et al. 2007). This study presents a detailed examination of chemical leaching and its relationship to secondary clay mineralogy in a basalt saprolite.

The Columbia River Basalts (CRB) are continental flood basalt lavas located in the interior northwestern United States including portions of Washington, Oregon, and Idaho (Tolan et al. 1989; Reidel et al. 2013). The majority of these lavas were erupted during the mid-Miocene Climatic Optimum, when the climate of the northwestern United States was considerably warmer and wetter than in the present day (Takeuchi and Larson 2005). Lava flows exposed at the surface weathered rapidly under these conditions to form soils. Those soils were later covered by younger lava flows, preserving the buried saprolites and paleosols as records of past climatic conditions (Sheldon 2003; Takeuchi and Larson 2005; Sheldon 2006; Hobbs and Parrish 2016). Although some overprinting occurred where the capping lava flows reacted with the capped soils (Baker 2017), the paleosols and their underlying saprolite zones also preserve a record of the weathering reactions that converted basalt flows to soils. Weathering of CRB is considered to have significantly contributed to both fixation of atmospheric CO_2 and the flux of dissolved ions to the world's oceans via the Columbia River system (Taylor and Lasaga 1999).

The fixation of carbon and the flux of dissolved ions from a weathering basalt will depend upon the individual weathering reactions occurring in the surface and subsurface. A number of studies have examined the chemistry and mineralogy of basalt weathering (Colman 1982; Eggleton et al. 1987; Nesbitt and Wilson 1992). These studies show that weathering trends of element depletion and preferential mineral dissolution vary from system to system. The early weathering behavior of individual rocks is controlled by their primary mineralogy and by the microstructural properties that control water movement through the rock (Meunier et al. 2007), with element leaching being diffusion-limited until porosity reaches ~9% (Navarre-Sitchler et al. 2009; Navarre-Sitchler et al. 2013). Typically, olivine is the earliest-weathering phase if present, but the order of subsequent dissolution of glass and of minerals such as pyroxenes, plagioclase, and Fe-Ti oxides varies between different studies (Allen and Scheid 1946; Eggleton et al. 1987; Nesbitt and Wilson 1992). Element leaching from basalts is also subject to redox control, with Fe loss indicating anoxic or reducing conditions (Ohmoto 1996; Rye and Holland 1998; Rye and Holland 2000; Babechuk et al. 2014). Thus, element release from weathering of freshly emplaced basalts is likely to vary with time as different minerals undergo dissolution and as the zone of leaching moves progressively downward from the flow surface.

Element leaching from weathering basalts is accompanied by precipitation of secondary mineral phases. Fe-bearing smectites are typical secondary clays produced by early basalt weathering, transitioning to kaolinite / halloysite and Fe (oxyhydr)oxides in more extensively weathered samples (Glasmann and Simonson 1985; Eggleton et al. 1987; Vingiani et al. 2010). The first low-temperature weathering product of CRB is nontronite clay, sometimes accompanied by opaline silica and clinoptilolite (Benson and Teague 1982; Allen and Scheid 1946). Nontronite is a ferric smectite with nominal (Na-saturated) endmember composition $Na_{0.3}Fe_2(Si,Al)_4O_{10}(OH)_2{\cdot}nH_2O$. Previous studies have suggested that nontronite forms via basalt weathering only under conditions where water-rock interaction is limited (Ehlmann et al. 2011) and that it disappears completely from rocks as they undergo more pervasive alteration (Allen and Scheid 1946). However, Sherman et al. (1962) observed nontronite accompanying bauxite in highly weathered basalt from Hawaii, and suggested it might persist longer than was thought under extensive weathering. Coexisting nontronite and halloysite or kaolinite have since been described by several other studies of basalt weathering. Vingiani et al. (2010) observed nontronite + kaolinite/halloysite replacing feldspars in weathering basaltic pebbles in soil, and de Oliveira et al. (1998) described it in a transitional zone of intermediate weathering between saprock and soil. Cravero et al. (2014) described it in altered ignimbrites, indicating it may also occur in rocks of silicic composition. These studies attributed the co-occurrence of ferric smectites and kaolinite / halloysite to local variations in porosity and permeability that allowed secondary mineral compositions to be controlled locally by dissolution. It is not clear whether any of the clays described were Fe-bearing mixed-layer kaolinite-smectite phases, which may also form via basalt weathering, and the compositions of which are also subject to local controls on solution chemistry (Le Blond et al. 2015).

These observations suggest that both element leaching and secondary mineral formation during basalt weathering are intimately tied to hydrologic conditions in the rock (Meunier et al. 2007; Navarre-Sitchler et al. 2011), not only during early weathering but well into intermediate-stage weathering in which significant desilication is occurring. Therefore, secondary clay mineralogy in saprolites may serve as an indicator of how hydrologic connectivity developed, and how element leaching progressed, during the weathering process.

The purpose of this study was to examine weathering along a depth transect through a basaltic saprolite, and to assess the primary minerals undergoing dissolution, major rock components undergoing leaching, and clay and secondary minerals being formed. A previous study (Baker 2017) presented whole-rock chemical data and bulk XRD data along this transect that showed chemical patterns resulting from weathering (Table 1). This study presents complementary element maps and synchrotron-based microanalyses examining the individual reaction zones where alteration reactions were preferentially leaching certain elements and minerals from the rock, and where secondary clay minerals were precipitating from the weathering fluids. These data provide information on element release over time from weathering Columbia River Basalts, and on the stability of nontronite during closed- and open-system weathering.

The questions of element leaching and secondary mineral formation during weathering are also of considerable interest on Mars, where the presence of extensive clay mineral deposits in ancient rocks indicates that aqueous weathering may have taken place in the planet’s ancient past (Bibring et al. 2006; Mustard et al. 2008; Murchie et al. 2009; Bishop et al. 2013; Carter et al. 2015). Terrestrial basalt weathering systems are useful possible analogs for rock alteration and clay formation on Mars (Greenberger et al. 2012; Thomson et al. 2014; Greenberger et al. 2015). This system presents a likely geochemical parallel to terrestrial basalt weathering in terms of the release of dissolved ions, carbonate fixation, and possibly climate feedbacks. A better understanding of rock weathering and the formation of secondary clay minerals under different climatic conditions will improve interpretation of the martian clay mineral deposits. If saprolite secondary mineralogy preserves information about weathering conditions and element leaching, then future close study of the secondary mineralogy of martian saprolites may provide detailed information on crustal hydrology, element cycling, and weathering-controlled climate feedbacks on early Mars.

Methods

Sample collection

The sample locality near Trinidad, WA was previously described by Baker (2017) and further details of the regional geology are given in that study. At this locality, a saprolite overlain by a thin (~50 cm) paleosol is developed on the Basalt of Gingko, and capped by a flow of the Basalt of Sand Hollow, both units of the Frenchman Springs Member of the Wanapum Basalts of the Columbia River Basalts (Tolan et al. 2009). The saprolite was sampled at depths of 10, 15, 20, 30, 60, and 80 cm below the contact between the capping basalt and the paleosol top. Fresh Gingko basalt was not exposed at the transect site, so an unweathered sample was collected from an exposure downslope.

In the laboratory, secondary mineral infillings were scraped or picked by hand from void spaces in the 80 cm saprolite sample for separate spectroscopic analysis. These infillings were sorted on the basis of color and included tan, brown, and black samples. Upon sampling it was found that the so-called black clay actually consisted of a brown infill with a brittle, black exterior coating; however, this sample was analyzed separately and will be referred to throughout this study as the black clay sample. Multicolored secondary mineral infillings were also observed in the 60 and 30 cm saprolite samples, but it was not possible to collect sufficient amounts of these clays for separate analysis.

Analytical methods

Details of bulk chemical and mineralogical analysis, and the results of these analyses, are given by Baker (2017). The bulk chemical data from that study are presented in Table 1, with additional data on C and Zr concentrations and calculated weathering indices.

Bulk saprolite samples from each depth were crushed by hand using a mortar and pestle and were analyzed by Fourier transform infrared spectrosopy (FTIR). Each sample was mixed with optical-grade KBr at a clay:KBr ratio of 3:100 and analyzed on a Perkin-Elmer System 2000 spectrometer with diffuse reflectance accessory. FTIR spectra were processed using the Kubelka-Munk algorithm provided in Perkin Elmer Spectrum 2.0 software.

Paleosol and saprolite samples were impregnated with Petropoxy under vacuum for thin-section preparation. Many of these samples contained a large amount of pore space (primary vesicle space, or voids expanded by dissolution), but were not high permeability (due to a lack of interconnection between void spaces), which made complete epoxy impregnation challenging. As a result of this, of the extreme friability of these samples, and of the need to preserve the delicate spatial structures of secondary minerals infilling void spaces, multiple impregnation steps were used to stabilize the samples before and between individual cutting and polishing steps.

Carbon-coated thin sections were analyzed at the Washington State University GeoAnalytical Laboratory on a JEOL 8500F field-emission electron microprobe. Backscattered electron images and wavelength-dispersive X-ray maps, showing the relative distribution of individual elements within the mapped area, were collected of secondary mineral infills and their spatial relationships with the parent basalt. Because the secondary clay minerals in the samples tended to pluck during polishing, resulting in a poorly polished surface, quantitative analyses of clay composition were not performed.

Thin sections of all samples were taken to Stanford Synchrotron Research Laboratory (SSRL) for synchrotron-based microanalysis on Beamline 2-3. Selected sample regions were element mapped by μ-X-ray fluorescence (μ-XRF) with an incident beam energy of 7500 eV, tuned with a Si(111) monochromator. Electron beam energy was 3 GeV and beam current was 350 mA. Beamline 2-3 uses Kirkpatrick-Baez Pt-coated focusing optics to achieve a beam spot size as small as 2 by 2 μm. Thin sections were attached to an XYZ stage oriented 45° to the beam. The fluorescence yield was detected using a single channel Vortex Si detector. Element maps were collected using a 2 μm spot size and a dwell time per point of 250 milliseconds. The μ-XRF data were analyzed and the maps were produced using the software package SMAK version 1.1 (Webb et al. 2011). The regions mapped by μ-XRF were selected to overlap those previously mapped by electron microprobe. Selected spots of interest, chosen due to their relatively high Fe content, were analyzed by μ-X-ray absorption near edge spectroscopy (μ-XANES) at the Fe K-edge. Three to four spectra from each spot were aligned and averaged using the software package SixPack version 1.3 (Webb 2005).

Subsamples of three hand-picked clay infillings from the 80 cm saprolite sample were analyzed by extended X-ray absorption fine structure spectroscopy (EXAFS) at SSRL Beamline 7-3. These samples were crushed and rubbed in an even layer on filter paper (Whatman #2). The sample-impregnated filter paper was cut into strips, stacked three layers deep in a sample holder, and held in place with Kapton tape. The monochromator for this beamline consisted of two parallel Si(220) crystals with a 6-mm entrance slit. All samples were run in a liquid He-cooled cryostat at a temperature of 10 K. Fluorescence data were collected using a passivated implanted planar silicon (PIPS) detector. One to three EXAFS scans per sample were calibrated to a standard Fe foil and averaged using SixPack (Webb 2005). Processing and shell fitting were carried out using the programs Athena and Artemis (Ravel and Newville 2005). Shell fitting was performed using the method described by Baker and Strawn (2012), to confirm that the brown and tan clay infillings were typical of high-Fe nontronites with similar bond distances and parameters.

Results

Hand samples and mineralogy

The Gingko parent basalt contained plagioclase phenocrysts, with abundant quench-textured acicular plagioclase and skeletal Fe-Ti oxides within a finely textured groundmass. No olivine or pyroxene phenocrysts were present in this flow. This is consistent with previous descriptions of this basalt (Martin et al. 2013) and with results from bulk XRD analysis (Baker 2017).

Samples from 20-80 cm deep in the saprolite were medium to light gray in appearance, progressively lighter-toned at shallower depths, and contained considerable void space. The bulk mineralogy of these samples was dominated by primary plagioclase feldspar and minor titanomagnetite, with a small admixture of secondary smectite and, at 20 cm, kaolinite (Baker

2017). Bulk FTIR analyses indicate that the clay mineral halloysite was also present in samples from depths of 30-80 cm (Figure 1).

Open void spaces were observed in saprolite samples from 20-80 cm depth. Some void spaces contained no obvious secondary minerals. Some spaces exhibited partial interior coatings of tan, brown, green, or black minerals, with the different colors appearing in different void spaces. Black terminal coatings were sometimes present on tan or brown clay infillings, but the black material was never coated by clay minerals of other colors. In many cases, these partial interior coatings had a mossy, vermicular appearance (Figure 2), with tendrils extending from the void edge into its interior. These tendrils are observable in thin sections where they were preserved by epoxy impregnation. Other void spaces were completely filled with clay of uniform tan or brown color.

Samples from 10 and 15 cm below the contact were visually different from those below; they exhibited a streaky white and pale green mottling. Open or obviously infilled void spaces were not observable in these samples, although their epoxy consumption during thin sectioning suggested they had relatively high porosity. Bulk XRD results indicated that plagioclase feldspar was absent from these samples and that the dominant mineral present was a smectite (Baker 2017). Clay separates from these depths were smectites with d-spacings of 14.7 – 15 Å (Mg-saturated), expanding slightly upon glycerol solvation (15-15.5 Å), and collapsing upon K-saturation (13-13.2 Å) and subsequent heating (10 Å). The relatively small expansion upon glycerol solvation suggests this smectite may have high layer charge. Alternatively, interlayer hydroxide precipitates could be present in the sample, preventing complete glycerol penetration (Barnhisel and Bertsch 1989; Harris and White 2008).

Bulk chemical trends and weathering indices

Bulk chemical analyses of the parent basalt and saprolite samples were presented by Baker (2017) and are shown in Table 1. Also shown are the oxidizing and reducing mafic index of alteration (MIA-O and MIA-R respectively) (Babechuk et al. 2014). Table 2 shows mobility ratios (τ) (Brimhall et al. 1992; Sheldon 2003) calculated with respect to Zr from the data in Table 1 corrected to an anhydrous basis. The mobility ratio compares abundance of an element in a given sample to its abundance in the parent rock. The concentration of the element of interest is ratioed to the concentration of a supposedly immobile element. Calculation of mobility ratios with respect to Zr thus includes an assumption that Zr remains immobile throughout weathering; this behavior has been observed for weathering of other Columbia River Basalts (Thomson et al. 2014) but, from the bulk chemical data in Table 1, is clearly not appropriate at Trinidad for depths shallower than 20 cm, and ratios calculated for 0-15 cm should be treated with caution. No elements analyzed were observed to remain immobile in the Trinidad saprolite. Elements often treated as immobile in weathering systems include Zr, Ti, and Al. All of these elements become mobile in the Trinidad saprolite above 20 cm (Tables 1 and 2) and calculations of τ for the Trinidad samples with respect to each of these three elements yielded similar values.

These data show that at 80 cm depth, the majority of Mg and K had already been leached from the rock along with some Ca, Si, and Fe. This leaching trend progressed up-section to 20 cm. Elements including Al, Ti, Na, and P as well as many trace elements were relatively immobile at these depths, and passively accumulated as other elements were leached. This observation is consistent with dissolution of any glass present and of ferromagnesian groundmass minerals. The immobility of Al in combination with the detection of halloysite suggests that any Al leached from aluminous phases such as plagioclase was immediately re-precipitated. At 10-15 cm depth, loss of P, Ti, and Zr indicates dissolution of refractory phases such as apatite and titanomagnetite, but other elements appeared to have been enriched with respect to the deeper saprolite layers. In the paleosol, elements including Fe, Si, and particularly Mn were enriched to higher values than in the parent basalt. This enrichment likely arose due to chemical reaction with the overriding basalt, mediated by hydrothermal circulation of soil water (Baker 2017).

Electron microprobe element mapping

The electron microprobe images and element maps show that primary minerals present included plagioclase and titanomagnetite, in agreement with the previously published observations from bulk chemistry and XRD. At 80 cm below the surface, large void spaces were lined and small void spaces were filled with clay minerals. These clays exhibited a vermicular texture (Figure 2). Compositionally zoned Fe-rich clays lined the contact between groundmass and clay infill, and individual clay tendrils had Fe-rich, Mg-poor cores (Figure 3). These early clays were coated with alternating bands of relatively Mg-rich and relatively Mg-poor clays (Figure 4). In some void spaces, the clay coating was terminated by a layer of black Mn oxides (Figure 3). Most void spaces were coated rather than completely filled by clays, but some clay-filled embayments penetrated the walls of the void spaces, apparently having formed by dissolution of more soluble groundmass components (Figure 5).

At 60 cm below the surface, textural evidence suggested continued preferential dissolution of ferromagnesian components. Relict plagioclase crystals projected into open void spaces and were coated with Fe-Mg clay minerals (Figure 6). Although plagioclase showed textural evidence of some dissolution, the crystals were largely intact and maintained their overall lath-like shape and sharp boundaries. The texture of intact plagioclase laths projecting into open void spaces, and of open void spaces with square terminations against plagioclase crystal edges, suggests the void spaces were formed around the crystals by preferential dissolution and partial removal of the matrix around them, leaving the clay precipitates behind. As in the 80 cm sample, these clays were zoned in Fe and Mg.

At 30 cm, evidence appeared for partial dissolution of plagioclase in addition to ferromagnesian minerals. Plagioclase crystals no longer projected into void spaces, but terminated against intricately zoned clay infillings. Void spaces were lined with layered Fe-Mg clays as in deeper samples, but distinct Al-rich zones were also present in the clay linings (Figure 7). These Al-rich zones defined a boundary between the layered Fe-Mg clay infillings and more morphologically complex Fe-Mg clays that appeared to be possibly pseudomorphic after parent mineral(s). These may define the edges of crystals that were originally clay-coated but unaltered (Figure 6), and they indicate that the clay-filled zones of alteration expanded outwards into the rock mass from the boundaries of the originally clay-lined or clay-filled void spaces.

At 20 cm below the surface, the texture changed from rock with localized altered zones to a pervasively recrystallized appearance. Relict plagioclase phenocrysts showed abundant evidence of dissolution (Figure 8). Quench-textured Fe-Ti oxide crystals disappeared from the groundmass and were replaced by a Mg-rich phase, possibly a smectite. Aluminous zones became more prominent in clay void infills. The Fe-Mg-rich clays filling the older void spaces were still present, but were now surrounded by aluminous secondary clay minerals. This sample appeared to represent a transition state between leaching of ferromagnesian components and removal of aluminosilicate and less mobile components, and from precipitation of Fe-rich clays to precipitation of aluminous clays.

At 10-15 cm below the surface, open void spaces such as were present deeper in the section were absent. Minor Fe clays were present in isolated pockets (Figure 9), but most Fe-rich zones were Si-poor. An Fe-rich phase was present as lacy coatings or infills and was free of Si or other elements, suggesting a hydroxide or oxide phase. Aluminous clay minerals were pseudomorphic after plagioclase laths (Figure 9 upper right), or Al-Mg clays alternated in bands with an Fe-rich, Si-poor phase (Figure 9 upper left).

X-ray absorption spectroscopy

Synchrotron-based X-ray absorption (XAS) data including bulk EXAFS and μ-XANES spectra were used to help identify Fe-rich secondary minerals present in the clay infillings. Fe K-edge XAS spectra are a sensitive indicator of Fe valence, speciation, and structural environment in crystalline and non-crystalline materials (Waychunas et al. 1983; Wilke et al. 2001; O'Day et al. 2004; Wilke et al. 2007). They are also useful for distinguishing phyllosilicates from oxides and other major Fe-bearing phases (Baker et al. 2010), for distinguishing between dioctahedral and trioctahedral phyllosilicates (Finck et al. 2015), and for analyzing cation content and distribution in clay minerals (Manceau et al. 1988; Vantelon et al. 2003; Baker and Strawn 2012). The use of synchrotron microprobe XRF and XANES analysis in particular allows in-situ identification of very small or low abundance phases that cannot be analyzed in bulk.

The tan, brown, and black clay infillings that were handpicked from the 80 cm sample were available in sufficient quantity for bulk XAFS analysis (Figure 10). These bulk samples are likely to be mixtures of the compositional range of zoned clays observed by electron microprobe (Figures 2-4). The black clay corresponds to the infillings observed by electron microprobe to be Fe-rich clays coated with black Mn oxides (Figure 3). The EXAFS spectra of all these samples resembled those of nontronite standards and were typical of high-Fe clays; the spectrum of UI-Garfield nontronite (Baker and Strawn 2012), a high-Fe ferric nontronite, is shown in Figure 10 for comparison. Spectra of the tan and brown samples were very similar to one another, with only a few minor differences that may correspond to slight variations in composition. If other secondary phases were present such as high-Al or high-Mg smectites, trioctahedral smectites such as saponite, or other Fe-rich phases such as (oxyhydr)oxides, their presence would be evident in the XANES and EXAFS spectra. No such phases were detected in the bulk samples from 80 cm, only high-Fe nontronite. The presence of some phases such as Fe (oxyhydr)oxides would be evident from unique features in the XANES spectra (Figures 9a and 9b), whereas the presence of trioctahedral smectites or of compositionally heterogeneous dioctahedral smectites would be apparent from shifts in the XAFS oscillations (Figure 10c) and from changes in peak location and intensity in the Fourier transformed spectra (Figure 10d).

The Fe edge in the near-edge portion of the black clay spectrum contained a lower energy shoulder at 7120 eV that was not present in the spectra of the tan and brown clays and the nontronite standard; this inflection was more obvious in the first derivative of the spectrum (Figure 10b, arrow). This feature suggests that some Fe(II) was present in this clay sample (Waychunas et al. 1983) . The XANES and EXAFS spectra were otherwise similar to those of high-Fe nontronite samples, except that the black clay XAFS spectrum had a lower amplitude than the tan, brown, and Garfield clay spectra (Figure 10c and 10d), suggesting this clay may also be somewhat less ordered.

μ-XRF and XANES

The tan, brown, and black clays described above were collected from the same hand samples that were thin-sectioned and probed using μ-XRF and XANES. Because they represent the same population of secondary minerals, they were used in this study as spectroscopic standards for interpretation of the microbeam data. This is particularly useful for the Fe(II)-

containing clays with black Mn-rich coatings, as similar clays have not, to our knowledge, been previously described.

The point XANES spectra of clay coatings from the 60 and 80 cm samples (Figure 11) were nontronite-like, and most resembled the bulk XANES spectrum of the black clay, including the reduced Fe shoulder at 7120 eV as described in the previous section. This strongly suggests that most of the clay coatings analyzed contained similar amounts of Fe(II) to the black clay, and that the fully oxidized tan and brown clays were not typical of the clays analyzed by point analysis. However, some beam-induced reduction of Fe may have also occurred in these samples, as the microprobe XANES spectra were collected at room temperature whereas the bulk XAFS spectra were collected at 10 K.

One XANES spectrum was deliberately collected on a primary Fe-Ti oxide from the 80 cm sample. Although this spectrum resembled a hematite standard spectrum in its overall shape (Figure 12), the very high pre-edge peak and the position of the first main edge inflection (7120 eV) more closely matched that of the magnetite spectrum. As in the black clay, the inflection at 7120 eV indicated the presence of some Fe(II) in this sample. Hematite was not a primary phase in the basaltic parent rock, whereas titanomagnetite was, and was detected in this sample by XRD (Baker 2017). Therefore this spectrum will be taken as typical of primary titanomagnetite in the parent basalt. All but one of the point XANES spectra collected from the 30 cm sample (Figure 12) partly matched the XANES spectrum of this titanomagnetite. The remaining, non-oxide-like spectrum from 30 cm resembled that of the brown clay. Two of the oxide-matching points had very large pre-edge features (position indicated by arrow on Figure 12) and best matched the titanomagnetite spectrum from the 80 cm sample. The other two had relatively small pre-edge features similar to clay mineral pre-edges rather than the large pre-edge features typical of Fe oxide and hydroxide minerals; however, their main edge features were similar to the titanomagnetite main edge and not to clay spectra. Those two spectra did not perfectly match any single standard.

All but two point XANES spectra collected from the 20 cm sample resembled the black clay spectrum and were indistinguishable from Fe-rich clay XANES spectra collected on the deeper samples (Figure 13). This indicated that nontronite was still present in this kaolinite-bearing sample. The two spectra (shown lowest on Figure 13) from the 20 cm sample that did not match clay spectra do not have distinctive edge features, suggesting they may be poorly crystalline phases such as Fe (oxyhydr)oxides. Point XANES spectra collected from the 10 cm sample best match that of the hematite standard (Figure 14).

Discussion

Patterns of mineral dissolution, chemical depletion, and clay formation

Between the parent basalt and the deepest 80 cm saprolite sample, Al, Ti, P, and Zr appeared to behave in a conservative manner (Table 1). Most other major elements appeared to have undergone some leaching from the bulk rock, whereas volatile components (H_2O and C; Tables 1 and 2) were added. The most mobile elements at this depth were Mg and K; the 80 cm sample is depleted of 80% of the K_2O and 77 % of the MgO that were present in the parent rock. Less depleted but still mobile elements included Ca (43 % CaO leached), Fe (33% Fe_2O_3), Si (30 % SiO_2), and Na (20% Na_2O) (Table 2). Overall, at the 80 cm mark, 28% (calculated on a volatile-free basis) of the rock's mass had been removed by leaching. This calculation assumes Zr behaved in a completely conservative manner, but similar numbers are arrived at using Ti and

Al contents. The volatile content of this rock is dominated by H_2O (Table 1) and are likely primarily due to its clay content. The nontronite clay present as linings and infillings in void spaces represents elements (mostly Fe and Si, with minor Mg) that were leached from primary minerals but were redeposited rather than being lost to groundwater. The depletion of these elements in the bulk rock, and the presence of relatively thin secondary smectite coatings, shows that formation of the brown and tan secondary nontronite coatings does not account for all of the Fe and Si leached from the parent rock. By contrast, as noted above, the presence of halloysite and the immobility of Al suggests that any Al liberated from aluminous phases such as plagioclase was immediately re-precipitated in this clay mineral.

Between 30 and 80 cm depth, sample bulk chemistry indicated ongoing removal of ferromagnesian minerals (loss of Mg, Fe, and Ca) and passive accumulation of Al, Ti, P, and remaining alkalis. This is consistent with the observation by XRD and EPMA that groundmass was leached but plagioclase feldspar was mostly unaltered at these depths. Some plagioclase crystals immediately around void spaces did show evidence of dissolution in the sample from 30 cm depth (Figure 7). As minimal depletion of Al was observed in this sample (Table 2), it appears that Al released by feldspar dissolution was immediately precipitated in the Al-rich, Fe-poor clay layers that were also observed in this sample (Figure 7).

As discussed above, two point XANES spectra from the 30 cm sample had large main edge features resembling the titanomagnetite standard, but small pre-edge features more similar to clay minerals. The identity of these mineral phases is unclear. These spectra could indicate primary minerals undergoing alteration and intimately mixed with a secondary phase, or they could be mixtures produced by analyzing thin clay coatings over embedded Fe-Ti oxides. The XANES points from the 30 cm sample were all located on what appeared to be clay coatings similar to the coatings in the deeper samples. However, any Fe oxides embedded in the clay coatings (such as the clay coated titanomagnetites visible in Figure 6, and the titanomagnetites embedded in the clay near the clay-groundmass boundary in Figure 7) would have contained the highest mapped Fe contents and would therefore have presented likely targets for point analysis.

The total volatile content (LOI; Table 1) of the samples from between 30 and 80 cm did not vary with depth, suggesting that the total clay mineral content also did not vary up-gradient through this depth interval. Weathering in this depth range therefore appears to have primarily taken the form of leaching of chemical components and precipitation of secondary minerals including halloysite and nontronite.

By the 20 cm depth interval, 42% of the rock (by mass) had been removed by progressive leaching, calculated on a volatile-free basis assuming Zr was completely conservative. Plagioclase dissolution was observed in electron microprobe images of this sample (Figure 8), and aluminous zones became more prominent in smectite clay linings. Element maps showed that Fe-Ti oxides had been replaced by a Mg-rich phase (Figure 8), possibly a clay such as montmorillonite. The bulk rock Al and Ti contents peaked at this depth (Table 1), indicating that although these elements' host minerals such as feldspar and titanomagnetite were being etched (Figure 8), the elements themselves had not been leached from the bulk rock. The volatile content of this sample was higher than those beneath it (Table 1), indicating a higher clay mineral content, which may account for a portion of the Al that had been leached from plagioclase but was not lost from the rock. A broad 7 Å inflection seen in XRD patterns suggests kaolinite may be present at this depth in addition to smectite (Baker 2017). Isolated Ti-rich zones (Figure 8) may indicate that Ti from oxides was transported only on the micron scale, and re-precipitated as oxides.

The 20 cm sample thus appears to represent a turning point in the weathering evolution of this basalt, from leaching of ferromagnesian groundmass components to leaching of all primary phases including feldspar, titanomagnetite, and apatite. It contained both nontronite and kaolinite, suggesting that clay mineralogy was still controlled by local porosity at this stage, but that open-system leaching was initiating in portions of the weathering rock. This sample also represents the point above which none of the elements analyzed behaved in a conservative manner, so that mass losses above this depth can no longer be evaluated quantitatively. However, the extensive leaching of all primary phases, and the fact that 30-40% of the rock mass had already been previously lost from the rock, suggest that the majority of the initial basalt mass (and volume) had likely been leached from this sample. It is therefore not surprising that the transition to a very different mineral assemblage occurs within a few cm.

No relict primary basaltic mineral phases were observed in the sample from 10 cm. Lacy Fe oxides were observed in this sample (Figure 9) and Fe-rich clays were not, suggesting it is likely that hematite is the predominant Fe-bearing phase in this sample. An increase in LOI indicated increased accumulation of clay minerals, and bulk XRD analysis indicated that a smectite was abundant in this sample (Baker 2017). However, none of the XANES point spectra resemble the spectrum of Fe in a clay mineral, suggesting that smectites in this sample are all low-Fe in composition. Blocky concentrations of lacy Fe oxides and of aluminosilicates, probably clays, appeared to be pseudomorphic after feldspar laths (Figure 9). The XANES spectra from this sample indicated that high-Fe spots contained hematite rather than a clay mineral. However, the shallow saprolite and paleosol samples have been geochemically altered by reaction with the capping basalt flow and Si-rich sediments, and contain excess Fe, Si, Mg, and Mn (Baker 2017). The mineral phases containing these elements are likely to partly reflect formation in a contact metamorphic environment rather than a pedogenic environment.

Open system vs closed system alteration

It has been proposed that nontronite clay forms by alteration of mafic parent rocks under closed-system conditions, whereas open-system alteration is dominated by leaching of mafic components such as olivine (Ehlmann et al. 2011) . The results presented here suggest that there is not a sharp distinction between closed nontronite-forming systems and open leaching-dominated systems, because the two processes may be contemporaneous where water-rock ratio is limited.

A completely closed system is not likely to be a common occurrence in nature. In the case of aqueous weathering of basalt, unless alteration solely involves magmatic fluids (Meunier et al. 2012), the system must at least be sufficiently open to permit the altering fluids to enter. However, where fluid transport is limited by permeability, fluid chemistry will be controlled by equilibrium with the mineral phases present (Navarre-Sitchler et al. 2011) and overall water-rock ratio will be low. These are probably the conditions implied by “poor drainage” – the description used by Allen and Scheid (1946). Nontronite formation is promoted by anoxic or reducing conditions and relatively high pH (Harder 1976), conditions that suggest that fluid chemistry is controlled by basalt dissolution. The behavior of Fe in solution is strongly affected by oxidation state, because the solubility of Fe(II) is much greater than that of Fe(III). As a result, Fe will leach from the weathering rock under anoxic conditions, whereas under oxidizing conditions it will be retained as ferric oxides or hydroxides. To capture this difference, Babechuk et al. (2014) developed the Mafic Index of Alteration (MIA), a weathering index that includes mafic minerals containing Fe and Mg. The MIA can be separately calculated for oxidizing conditions (MIA-O), when Fe is treated as an immobile element, or for reducing conditions (MIA-R), when Fe is treated as a mobile element. As with other weathering indices, MIA values increase with increasing alteration of the rock; a specific increase in MIA-R values as opposed to MIA-O is indicative of Fe leaching.

At Trinidad, MIA-R values increased upwards in the transect from 80 to 20 cm (Table 1), whereas MIA-O values remained relatively steady. This suggests Fe was leached from the rock at depths greater than 20 cm, and therefore that conditions in the weathering fluid were anoxic or reducing below this depth.

The Trinidad samples from between 30 and 80 cm depth have lost 30-40% of the initial parent rock mass (assuming that Al, Ti, and Zr behave in a conservative manner) including Fe, Mg, and alkalis. Given this, the Trinidad weathering system cannot reasonably be described as closed; however, transport of fluid and dissolved ions out of the weathering system must have been sufficiently slow to permit intermittent nontronite saturation. The physical form of the nontronite as coatings and tendrils in open void spaces suggests that the clay may have precipitated from thin films of water coating rock surfaces. A reasonable physical model for the nontronite forming system at Trinidad would be periodic water saturation followed by slow drainage of porewater to the groundwater system. Precipitation of clay minerals from successive pulses of porewater would be consistent with the oscillatory zoning observed in the Mg and Fe content of the clay linings, which suggest that the fluid composition was not continuously buffered by equilibrium with dissolving primary phases.

Although the Trinidad nontronite-forming system was not closed to leaching of major components, it appears to have coexisted with the primary basaltic mineral assemblage as long as that assemblage remained. The appearance of more aluminous smectites and the disappearance of nontronite coincided spatially with the onset of dissolution of more resistant phases including feldspar, apatite, and titanomagnetite. In the Trinidad saprolite transect, this transition took place in a relatively narrow zone between 10 and 20 cm depth. The stable neoformed Fe phase above 20 cm depth appeared to be hematite (Figure 9), indicating that weathering conditions changed from anoxic to oxic across this transition zone. Extensive leaching of most analyzed elements from the 10-15 cm samples (Table 1) suggest that the onset of oxidizing weathering conditions corresponded with an increase in water-rock ratio. Future work examining stable isotope ratios may illuminate this further.

Initially, the primary rock porosity consisted of vesicles and a network of cooling cracks that effectively controlled rock permeability (Meunier et al. 2007; Mazurier et al. 2016). The cracks permitted limited transport of water through the rock and into vesicles, and limited transport of dissolved ions out of the weathering system. Over time, dissolution of the primary rock matrix and precipitation of clay infillings altered this primary permeability network. The nontronite-forming conditions would have existed for as long as drainage of porewater was limited by permeability. The transition from nontronite formation to formation of aluminous smectites, and from anoxic to oxic conditions, was therefore most likely controlled by the development of permeability in the weathering basalt and the transition to a completely open system.

Mass contributions to surface water over time

If the Trinidad saprolite is typical of weathering of CRB in the central Columbia Plateau, this suggests that emplacement of fresh basalt flows would have been followed first by an initial pulse of Mg and K to the groundwater system, then by slower release of Fe, Si, Na, and Ca. Although nontronite + halloysite was the stable clay mineral assemblage present during early weathering, relatively little leached Fe, Mg, or Si were retained as clay coatings within the rock, whereas dissolved Al was apparently precipitated immediately as halloysite. Precipitation of clays in cracks may have temporarily offset increases in subsurface permeability caused by leaching, as anoxic or reducing conditions persisted below the surface during leaching of approximately one third of the rock mass.

The switch to high water-rock ratio and to oxidizing conditions during subsurface weathering coincided, likely due to increased permeability as a result of continuing dissolution of the rock matrix. This later phase of weathering corresponded with release of Al, Ti, P, and associated alkalis by dissolution of more resistant phases including plagioclase, apatite, and titanomagnetite. Leaching of Fe ceased from the oxidized portion of the weathering column. Release of Al and Ti to groundwater would have been controlled by their limited solubility, but bulk chemistry suggests they were transported on at least a meter scale. This weathering transition is also marked by the appearance of aluminous smectites, minor kaolinite, and hematite as stable secondary phases. The sample from 20 cm depth appears to capture this transition point.

The transport and fate of dissolved ions released to groundwater through basalt weathering would depend on local hydrologic conditions. The present-day Columbia River is a gaining stream through much of the Columbia Plateau (Whitehead 1994), although local hydrologic connections between surface and groundwater can be complex due to the presence of many low-permeability layers (Burt et al. 2009; Lindsey et al. 2009; Lite 2013). In the late Miocene, much of this subsurface structure was in existence, but the surface hydrology of the

Columbia differed considerably from the present day. The emplacement of extensive CRB lava flows had repeatedly disrupted established drainages, damming and redirecting streams including the Columbia (Reidel and Tolan 2013). Redevelopment of drainages was affected by ongoing tectonism as well as the architecture of the newly emplaced basalt. During late Wanapum time (circa 14.5 Ma), the time period of weathering at Trinidad, the Columbia's course through the western Columbia Plateau apparently consisted of a series of interconnected shallow lakes rather than a well-developed river channel (Reidel and Tolan 2013). Interbedded sedimentary deposits indicate wet surface environments in the immediate vicinity of the Trinidad paleosol (Ebinghaus et al. 2014). Thus, communication between groundwater and surface water was likely complex during Wanapum time, and dissolved ions may have followed tortuous paths before discharging to the Pacific Ocean (Taylor and Lasaga 1999).

Potential applications to Mars

Some clay-bearing outcrops on Mars contain up to 55% nontronite as estimated from remote sensing (Poulet et al. 2008), much more of this clay than do any portions of the Trinidad saprolite. As discussed above, although nontronite is present in the Trinidad saprolite, the majority of Fe and Si dissolved from the parent basalt was lost to leaching rather than being redeposited in secondary phases. If the martian nontronite-forming system was more poorly drained than the Trinidad saprolite, then dissolved Mg, Fe, and Si may have re-precipitated in clay minerals, resulting in the high observed nontronite abundances. Although Fe-rich martian clays are often referred to in the literature as "nontronite", some spectra suggest these clays may contain both Fe(II) and Mg (Bishop et al. 2008), unlike typical terrestrial nontronites which dominantly contain Fe(III). At Trinidad, bulk compositions suggest very early leaching of Mg from the parent rock, and the Fe-Mg compositional banding observed in clay linings may preserve information about this phase of early weathering. Ongoing studies of very early-stage basalt weathering may help illuminate the relative timing of leaching and clay formation during this phase.

The clay-bearing outcrops on Mars may have formed by surface weathering in a pedogenic environment (Carter et al. 2015), although it has also been proposed that they may have formed under other conditions (Murchie et al. 2009; Ehlmann et al. 2011). If the aluminous clay outcrops are pedogenic in origin, then the relationships between leaching, element release, and clay formation at Trinidad may be useful in interpreting the sequence of events on Mars. At both high and lower abundance nontronite occurrences, the clay is accompanied by primary minerals such as plagioclase (Poulet et al. 2008); this is consistent with the observed saprolite mineralogy at Trinidad. Specific dissolution and leaching patterns of particular elements would have depended on the mineralogy of the parent rock undergoing weathering. Furthermore, as observed in ancient terrestrial soils formed before Earth's atmosphere became oxidized, soluble Fe(II) would be leached in a similar manner to Mg (Babechuk et al. 2014). However, the transition from Fe-Mg clays to aluminous smectites would still be expected to mark the transition to fully open-system weathering with loss of all primary mineral phases and extensive leaching of most elements.

Oxidized Fe compounds are present on the martian surface. Aqueous alteration observed in martian meteorites appears to have sometimes produced reduced phases such as siderite and sulfide minerals, suggesting alteration under moderately reducing conditions; however, other alteration assemblages contain ferric (oxyhydr)oxides, indicating more oxidizing conditions (Bridges et al. 2001). Therefore, iron may have been leached during weathering of martian rocks under some conditions. The chemical components leached from the parent basalt would have been released to the martian paleo-hydrologic system, perhaps ultimately contributing to the salt and oxide content of the present-day surface.

Implications

Patterns of element leaching and clay mineral deposition in a saprolite at Trinidad, WA show that precipitation of nontronite clay does not necessarily indicate weathering occurred in a chemically closed system; nontronite is stable even in rocks that have undergone significant leaching of major elements. Instead, formation of nontronite may indicate weathering under conditions of limited permeability. As permeability increases, aluminous clays such as kaolinite and/or montmorillonite become the stable secondary phase(s) present, but nontronite may persist in pockets of limited permeability. These observations suggest that the mineralogy and distribution of secondary clays formed by basalt weathering are likely to be strongly influenced by the initial physical characteristics of the basalt, such as the presence of cracks, joints, pillows, or other structures – many of which are in turn influenced by the conditions of lava emplacement. Release of dissolved ions and fixation of CO_2 may thus also depend on these factors.

The observed mineralogy of clay-bearing outcrops on Mars is consistent with similar patterns of mineral dissolution to those observed at Trinidad, although more detailed information on the martian outcrops is needed to determine whether saprolites are indeed a good analog for them. The high clay abundances observed in some martian outcrops may indicate more secondary mineral deposition and less element leaching (e.g., a more closed system) than observed in the Trinidad saprolite, suggesting that martian clay outcrops may preserve valuable information about martian hydrologic conditions in the ancient past.

Acknowledgements

We thank Sam Webb and Courtney Roach for support for synchrotron microprobe analyses on SSRL BL 2-3, Matthew Latimer and Erik Nelson for support for bulk XAS on BL 7-3, and Charlene Home and Archana Dahal for assistance with sample preparation and FTIR analyses. Thoughtful and constructive reviews by Javier Cuadros, Joel Hurowitz, and an anonymous reviewer provided the opportunity to significantly improve the manuscript. This research was partly funded by a seed grant from the Regents of the University of Idaho. Use of the Stanford Synchrotron Radiation Lightsource, SLAC National Accelerator Laboratory, is supported by the U.S. Department of Energy, Office of Science, Office of Basic Energy Sciences under Contract No. DE-AC02-76SF00515.

References

Allen, V.T. and Scheid, V.E. (1946) Nontronite in the Columbia River region, American Mineralogist 31, 294-312.

Babechuk, M.G., Widdowson, M. and Kamber, B.S. (2014) Quantifying chemical weathering intensity and trace element release from two contrasting basalt profiles, Deccan Traps, India, Chemical Geology 363, 56-75.

Baker, L.L. (2017) Formation of the ferruginous smectite SWa-1 by alteration of soil clays, American Mineralogist 102, 1, 33.

Baker, L.L. and Strawn, D.G. (2012) Fe K-edge XAFS spectra of phyllosilicates of varying crystallinity, Physics and Chemistry of Minerals 39, 8, 675-684.

Baker, L.L., Strawn, D.G., Vaughan, K.L. and McDaniel, P.A. (2010) XAS study of Fe mineralogy in a chronosequence of soil clays formed in basaltic cinders, Clays and Clay Minerals 58, 6, 772-782.

Barnhisel, R.I. and Bertsch, P.M. (1989) Chlorites and hydroxy-interlayered vermiculite and smectite, In Minerals in Soil Environments. Dixon, J. B. and Weed, S. B., Ed., pp. 729-788, Soil Science Society of America, Madison, WI.

Benedetti, M.F., Dia, A., Riotte, J., Chabaux, F., Gérard, M., Boulègue, J., Fritz, B., Chauvel, C., Bulourde, M., Déruelle, B. and Ildefonse, P. (2003) Chemical weathering of basaltic lava flows undergoing extreme climatic conditions: the water geochemistry record, Chemical Geology 201, 1–2, 1-17.

Bibring, J.-P., Langevin, Y., Mustard, J.F., Poulet, F., Arvidson, R., Gendrin, A., Gondet, B., Mangold, N., Pinet, P., Forget, F. and the Omega team (2006) Global mineralogical and aqueous Mars history derived from OMEGA/Mars Express data, Science 312, 5772, 400-404.

Bishop, J.L., Loizeau, D., McKeown, N.K., Saper, L., Dyar, M.D., Des Marais, D.J., Parente, M. and Murchie, S.L. (2013) What the ancient phyllosilicates at Mawrth Vallis can tell us about possible habitability on early Mars, Planetary and Space Science 86, 130-149.

Bishop, J.L., Dobrea, E.Z.N., McKeown, N.K., Mario Parente, Ehlmann, B.L., Michalski, J.R., Milliken, R.E., Poulet, F., Swayze, G.A., Mustard, J.F., Murchie, S.L. and Bibring, J.-P. (2008) Phyllosilicate diversity and past aqueous activity revealed at Mawrth Vallis, Mars, Science 321, 830-833.

Bridges, J.C., Catling, D., Saxton, J., Swindle, T., Lyon, I. and Grady, M. (2001) Alteration assemblages in martian meteorites: implications for near-surface processes, Space Science Reviews 96, 1, 365-392.

Brimhall, G.H., Chadwick, O., Lewis, C.J., Compston, W., Williams, I.S., Danti, K.J., Dietrich, W.E., Power, M.E., Hendricks, D. and Bratt, J. (1992) Deformational mass transport and invasive processes in soil evolution, Science 255, 5045, 695-702.

Burt, W., Conlon, T., Tolan, T.L., Wells, R.E. and Melady, J. (2009) Hydrogeology of the Columbia River Basalt Group in the northern Willamette Valley, Oregon, In Geological Society of America Field GuidesEd., pp. 697-736.

Carter, J., Loizeau, D., Mangold, N., Poulet, F. and Bibring, J.-P. (2015) Widespread surface weathering on early Mars: A case for a warmer and wetter climate, Icarus 248, 373-382.

Colman, S.M. (1982) Chemical weathering of basalts and andesites: Evidence from weathering rinds, Government Printing Office, Washington, DC. U.S. Geological Survey Professional Paper 1246 p.

Cravero, F., Marfil, S., Ramos, C. and Maiza, P. (2014) Coexistence of halloysite and iron-bearing clays in an altered ignimbrite, Patagonia, Argentina, Clay Minerals 49, 3, 429-441.

de Oliveira, M.T.G., Formoso, M.L.L., Trescases, J.J. and Meunier, A. (1998) Clay mineral facies and lateritization in basalts of the southeastern Parana Basin, Brazil, Journal of South American Earth Sciences 11, 4, 365-378.

Dessert, C., Dupré, B., Gaillardet, J., François, L.M. and Allegre, C.J. (2003) Basalt weathering laws and the impact of basalt weathering on the global carbon cycle, Chemical Geology 202, 3, 257-273.

Dupré, B., Dessert, C., Oliva, P., Goddéris, Y., Viers, J., François, L., Millot, R. and Gaillardet, J. (2003) Rivers, chemical weathering and Earth's climate, Comptes Rendus Geoscience 335, 16, 1141-1160.

Ebinghaus, A., Hartley, A.J., Jolley, D.W., Hole, M. and Millett, J. (2014) Lava–sediment interaction and drainage-system development in a large igneous province: Columbia River Flood Basalt Province, Washington State, USA, Journal of Sedimentary Research 84, 11, 1041-1063.

Eggleton, R.A., Foudoulis, C. and Varkevisser, D. (1987) Weathering of basalt; changes in rock chemistry and mineralogy, Clays and Clay Minerals 35, 3, 161-169.

Ehlmann, B.L., Mustard, J.F., Murchie, S.L., Bibring, J.-P., Meunier, A., Fraeman, A.A. and Langevin, Y. (2011) Subsurface water and clay mineral formation during the early history of Mars, Nature 479, 7371, 53-60.

Finck, N., Schlegel, M.L. and Bauer, A. (2015) Structural iron in dioctahedral and trioctahedral smectites: a polarized XAS study, Physics and Chemistry of Minerals 42, 10, 847-859.

Gaillardet, J., Dupré, B., Louvat, P. and Allegre, C. (1999) Global silicate weathering and CO2 consumption rates deduced from the chemistry of large rivers, Chemical Geology 159, 1, 3-30.

Gislason, S.R., Oelkers, E.H., Eiriksdottir, E.S., Kardjilov, M.I., Gisladottir, G., Sigfusson, B., Snorrason, A., Elefsen, S., Hardardottir, J. and Torssander, P. (2009) Direct evidence of the feedback between climate and weathering, Earth and Planetary Science Letters 277, 1, 213-222.

Glasmann, J.R. and Simonson, G.H. (1985) Alteration of basalt in soils of western Oregon, Soil Science Society America Journal 49, 1, 262-273.

Greenberger, R.N., Mustard, J.F., Kumar, P.S., Dyar, M.D., Breves, E.A. and Sklute, E.C. (2012) Low temperature aqueous alteration of basalt: Mineral assemblages of Deccan basalts and implications for Mars, Journal of Geophysical Research: Planets 117, E11.

Greenberger, R.N., Mustard, J.F., Cloutis, E.A., Mann, P., Wilson, J.H., Flemming, R.L., Robertson, K.M., Salvatore, M.R. and Edwards, C.S. (2015) Hydrothermal alteration and diagenesis of terrestrial lacustrine pillow basalts: Coordination of hyperspectral imaging with laboratory measurements, Geochimica et Cosmochimica Acta 171, 174-200.

Harder, H. (1976) Nontronite synthesis at low temperatures, Chemical Geology 18, 3, 169-180.

Harris, W. and White, G.N. (2008) X-ray diffraction techniques for soil mineral identification, In Methods of Soil Analysis. Part 5. Mineralogical Methods. Ulery, A. L. and Drees, L. R., Ed., pp. 81-115, Soil Science Society of America, Madison, WI.

Hobbs, K.M. and Parrish, J.T. (2016) Miocene global change recorded in Columbia River basalt−hosted paleosols, Geological Society of America Bulletin 128, 9-10, 1543-1554.

Kump, L.R., Brantley, S.L. and Arthur, M.A. (2000) Chemical weathering, atmospheric CO2, and climate, Annual Review of Earth and Planetary Sciences 28, 1, 611-667.

Le Blond, J.S., Cuadros, J., Molla, Y.B., Berhanu, T., Umer, M., Baxter, P.J. and Davey, G. (2015) Weathering of the Ethiopian volcanic province: A new weathering index to characterize and compare soils, American Mineralogist 100, 11-12, 2518-2532.

Lindsey, K., Morgan, D., Vlassopoulos, D., Tolan, T.L. and Burns, E. (2009) Hydrogeology of the Columbia River Basalt Group in the Columbia Plateau: Road log and field trip stop descriptions, In Geological Society of America Field GuidesEd., pp. 673-696.

Lite, K.E. (2013) The influence of depositional environment and landscape evolution on groundwater flow in Columbia River Basalt—Examples from Mosier, Oregon, Geological Society of America Special Papers 497, 429-440.

Maher, K. and Chamberlain, C.P. (2014) Hydrologic regulation of chemical weathering and the geologic carbon cycle, Science 343, 6178, 1502-1504.

Manceau, A., Bonnin, D., Kaiser, P. and Frétigny, C. (1988) Polarized EXAFS of biotite and chlorite, Physics and Chemistry of Minerals 16, 2, 180-185.

Martin, B.S., Tolan, T.L. and Reidel, S.P. (2013) Revisions to the stratigraphy and distribution of the Frenchman Springs Member, Wanapum Basalt, Geological Society of America Special Papers 497, 155-179.

Mazurier, A., Sardini, P., Rossi, A.M., Graham, R.C., Hellmuth, K.-H., Parneix, J.-C., Siitari-Kauppi, M., Voutilainen, M. and Caner, L. (2016) Development of a fracture network in crystalline rocks during weathering: Study of Bishop Creek chronosequence using X-ray computed tomography and 14C-PMMA impregnation method, Geological Society of America Bulletin 128, 9-10, 1423-1438.

Meunier, A., Sardini, P., Robinet, J. and Prêt, D. (2007) The petrography of weathering processes: facts and outlooks, Clay Minerals 42, 4, 415-435.

Meunier, A., Petit, S., Ehlmann, B.L., Dudoignon, P., Westall, F., Mas, A., El Albani, A. and Ferrage, E. (2012) Magmatic precipitation as a possible origin of Noachian clays on Mars, Nature Geoscience 5, 739-743.

Murchie, S.L., Mustard, J.F., Ehlmann, B.L., Milliken, R.E., Bishop, J.L., McKeown, N.K., Noe Dobrea, E.Z., Seelos, F.P., Buczkowski, D.L., Wiseman, S.M., Arvidson, R.E., Wray, J.J., Swayze, G., Clark, R.N., Des Marais, D.J., McEwen, A.S. and Bibring, J.-P. (2009) A synthesis of Martian aqueous mineralogy after 1 Mars year of observations from the Mars Reconnaissance Orbiter, Journal of Geophysical Research-Planets 114, E00D06.

Mustard, J.F., Murchie, S.L., Pelkey, S.M., Ehlmann, B.L., Milliken, R.E., Grant, J.A., Bibring, J.P., Poulet, F., Bishop, J., Dobrea, E.N., Roach, L., Seelos, F., Arvidson, R.E., Wiseman, S., Green, R., Hash, C., Humm, D., Malaret, E., McGovern, J.A., Seelos, K., Clancy, T., Clark, R., Marais, D.D., Izenberg, N., Knudson, A., Langevin, Y., Martin, T., McGuire, P., Morris, R., Robinson, M., Roush, T., Smith, M., Swayze, G., Taylor, H., Titus, T. and Wolff, M. (2008) Hydrated silicate minerals on Mars observed by the Mars Reconnaissance Orbiter CRISM instrument, Nature 454, 7202, 305-309.

Navarre-Sitchler, A., Steefel, C.I., Sak, P.B. and Brantley, S.L. (2011) A reactive-transport model for weathering rind formation on basalt, Geochimica et Cosmochimica Acta 75, 23, 7644-7667.

Navarre-Sitchler, A., Steefel, C.I., Yang, L., Tomutsa, L. and Brantley, S.L. (2009) Evolution of porosity and diffusivity associated with chemical weathering of a basalt clast, Journal of Geophysical Research: Earth Surface 114, F2.

Navarre-Sitchler, A.K., Cole, D., Rother, G., Jin, L., Buss, H.L. and Brantley, S.L. (2013) Porosity and surface area evolution during weathering of two igneous rocks, Geochimica et Cosmochimica Acta 109, 400-413.

Nesbitt, H.W. and Wilson, R.E. (1992) Recent chemical weathering of basalts, American Journal of Science 292, 10, 740-777.

O'Day, P.A., Rivera, N., Root, R. and Carroll, S.A. (2004) X-ray absorption spectroscopic study of Fe reference compounds for the analysis of natural sediments, American Mineralogist 89, 572-585.

Ohmoto, H. (1996) Evidence in pre–2.2 Ga paleosols for the early evolution of atmospheric oxygen and terrestrial biota, Geology 24, 12, 1135-1138.

Poulet, F., Mangold, N., Loizeau, D., Bibring, J.P., Langevin, Y., Michalski, J. and Gondet, B. (2008) Abundance of minerals in the phyllosilicate-rich units on Mars, Astronomy and Astrophysics 487, 2, 41-44.

Rad, S.D., Allègre, C.J. and Louvat, P. (2007) Hidden erosion on volcanic islands, Earth and Planetary Science Letters 262, 1, 109-124.

Ravel, B. and Newville, M. (2005) ATHENA, ARTEMIS, HEPHAESTUS: data analysis for X-ray absorption spectroscopy using IFEFFIT, Journal of Synchrotron Radiation 12, 4, 537-541.

Reidel, S.P. and Tolan, T.L. (2013) The late Cenozoic evolution of the Columbia River system in the Columbia River flood basalt province, Geological Society of America Special Papers 497, 201-230.

Reidel, S.P., Camp, V.E., Tolan, T.L. and Martin, B.S. (2013) The Columbia River flood basalt province: Stratigraphy, areal extent, volume, and physical volcanology, Geological Society of America Special Papers 497, 1-43.

Rye, R. and Holland, H.D. (1998) Paleosols and the evolution of atmospheric oxygen: a critical review, American Journal of Science 298, 8, 621.

Rye, R. and Holland, H.D. (2000) Geology and geochemistry of paleosols developed on the Hekpoort Basalt, Pretoria Group, South Africa, American Journal of Science 300, 2, 85.

Sheldon, N.D. (2003) Pedogenesis and geochemical alteration of the Picture Gorge subgroup, Columbia River basalt, Oregon, Geological Society of America Bulletin 115, 11, 1377-1387.

Sheldon, N.D. (2006) Using paleosols of the Picture Gorge Basalt to reconstruct the middle Miocene climatic optimum, PaleoBios 26, 2, 27-36.

Sherman, G.D., Ikawa, H., Uehara, G. and Okazaki, E. (1962) Types of occurrence of nontronite and nontronite-like minerals in soils, Pacific Science 16, 57-63.

Takeuchi, A. and Larson, P.B. (2005) Oxygen isotope evidence for the late Cenozoic development of an orographic rain shadow in eastern Washington, USA, Geology 33, 4, 313-316.

Taylor, A.S. and Lasaga, A.C. (1999) The role of basalt weathering in the Sr isotope budget of the oceans, Chemical Geology 161, 1–3, 199-214.

Thomson, B.J., Hurowitz, J.A., Baker, L.L., Bridges, N.T., Lennon, A.M., Paulsen, G. and Zacny, K. (2014) The effects of weathering on the strength and chemistry of Columbia River Basalts and their implications for Mars Exploration Rover Rock Abrasion Tool (RAT) results, Earth and Planetary Science Letters 400, 130-144.

Tolan, T.L., Reidel, S.P., Beeson, M.H., Anderson, J.L., Fecht, K.R. and Swanson, D.A. (1989) Revisions to the estimates of the areal extent and volume of the Columbia River Basalt Group, In Volcanism and Tectonism in the Columbia River Flood-Basalt Province. Reidel, S. P. and Hooper, P. R., Ed., pp. 1-20, Geological Society of America Boulder, CO.

Tolan, T.L., Martin, B.S., Reidel, S.P., Kauffman, J.D., Garwood, D.L. and Anderson, J.L. (2009) Stratigraphy and tectonics of the central and eastern portions of the Columbia River Flood-Basalt Province: An overview of our current state of knowledge, In Geological Society of America Field GuidesEd., pp. 645-672.

Vantelon, D., Montarges-Pelletier, E., Michot, L.J., Pelletier, M., Thomas, F. and Briois, V. (2003) Iron distribution in the octahedral sheet of dioctahedral smectites. An Fe K-edge X-ray absorption spectroscopy study, Physics and Chemistry of Minerals 30, 1, 44-53.

Vingiani, S., Terribile, F., Meunier, A. and Petit, S. (2010) Weathering of basaltic pebbles in a red soil from Sardinia: A microsite approach for the identification of secondary mineral phases, CATENA 83, 2–3, 96-106.

Waychunas, G.A., Apted, M.J. and Brown, G.E. (1983) X-ray K-edge absorption spectra of Fe minerals and model compounds: Near-edge structure, Physics and Chemistry of Minerals 10, 1, 1-9.

Webb, S., McNulty, I., Eyberger, C. and Lai, B. (2011) The MicroAnalysis Toolkit: X-ray fluorescence image processing software, AIP Conference Proceedings-American Institute of Physics 1365, 1, 196.

Webb, S.M. (2005) Sixpack: A graphical user interface for XAS analysis using IFEFFIT, Physica Scripta T115, 1011-1014.

Whitehead, R.L. (1994) Ground Water Atlas of the United States: Segment 7: Idaho, Oregon, Washington. U.S. Geological Survey Hydrologic Investigations Atlas HA-730-H: 31 p.

Wilke, M., Farges, F., Petit, P.-E., Brown, G.E., Jr. and Martin, F. (2001) Oxidation state and coordination of Fe in minerals: An Fe K-XANES spectroscopic study, American Mineralogist 86, 5-6, 714-730.

Wilke, M., Farges, F., Partzsch, G.M., Schmidt, C. and Behrens, H. (2007) Speciation of Fe in silicate glasses and melts by in-situ XANES spectroscopy, American Mineralogist 92, 1, 44-56.

Figure Captions

Figure 1: FTIR spectra of bulk saprolite samples, showing bulk clay mineralogy through the transect. In samples from depths of 30, 60, and 80 cm below the contact, halloysite is present as identified by peaks at 3695, 3620, 1100, 1035, and 915 cm^{-1}. Although smectites were identified in clay separates from these samples, smectite absorption bands are not identifiable in the bulk samples, suggesting halloysite is the more abundant phase. In samples from 10, 15, and 20 cm depth, characteristic absorption bands of nontronite (3565 and 815 cm^{-1}) and/or montmorillonite (3620, 875 cm^{-1}) are present.

Figure 2: Photo of vermicular tendrils in clay infilling in 80 cm sample (image 1 mm wide).

Figure 3: Clay tendril cross-section in 80 cm sample with relatively Fe-rich, Mg-poor center and Mn oxide coating.

Figure 4: Complex Mg-Fe zonation in clay infill in 80 cm sample. Images are 120 µm across.

Figure 5: Clay-filled embayment in vesicle edge in 80 cm sample. Brighter rings in Fe map (right) are cross-sections of vermicular tendrils with Fe-rich cores. Groundmass texture is also evident in this image, with skeletal Fe-Ti oxides.

Figure 6: BSE image of clay-lined vesicle in 60 cm sample, with clay-coated relict plagioclase laths and clay tendril cross sections (rounded / ovoid islands) and blocky embayments suggesting this void space was expanded by dissolution. Bright skeletal crystals are titanomagnetite.

Figure 7: Two examples of zoned clay coating in 30 cm sample, with complex Fe, Al, and Mg zonation.

Figure 8: Plagioclase dissolution and pervasive alteration of groundmass in 20 cm sample. Element maps do not overlap context map, but show a zoomed area of a nearby contact between original Fe-rich zoned clay infilling and altered groundmass. Patchy Ti distribution indicates dissolution of primary Fe-Ti oxides, and skeletal Mg pseudomorphs suggest replacement of Fe-Ti oxides by a low-Fe clay mineral.

Figure 9: Al-rich pseudomorph and feathery Fe oxides surrounded by Mg silicates in 10 cm sample.

Figure 10: XANES (a), first derivative of XANES (b), EXAFS (c), and Fourier transformed spectra (d) of picked clay infillings from 80 cm sample. Also shown is the UI-Garfield high-Fe nontronite (Baker and Strawn 2012) for reference. Inset in (a) shows pre-edge spectrum in greater detail. Arrow in (b) indicates reduced Fe shoulder. The Fourier transformed XAFS spectrum (d) shows peaks corresponding to atomic shells around an octahedrally coordinated Fe atom: six oxygen atoms at 2 Å, three first-neighbor Fe atoms at 3 Å and four Si neighbors at 3.25 Å, and additional backscattering O, Si, and Fe atoms at greater distances (Baker and Strawn 2012).

Figure 11: Synchrotron microprobe XANES (a) and first derivative of XANES (b) for high-Fe clays in 60 and 80 cm samples. Bulk spectra for brown and black clays are shown for comparison above and below point XANES spectra. Dotted line in (b) indicates reduced Fe shoulder observed in the black clay. These data show that the analyzed clays are all high-Fe nontronites. No Fe is present in an Al-rich or Mg-rich clay, a trioctahedral smectite, or in Fe (oxyhydr)oxides.

Figure 12: Synchrotron microprobe XANES (a) and first derivative of XANES (b) for titanomagnetite from 80 cm sample, hematite and magnetite standards, and high-Fe points in 30 cm sample (unlabeled curves). These results indicate that the analyzed high-Fe points in this sample likely contain primary titanomagnetite.

Figure 13: Synchrotron microprobe XANES (a) and first derivative of XANES (b) for high-Fe points in 20 cm sample and black clay separate. These results indicate that the high-Fe points analyzed in this sample contain a high-Fe nontronite with a reduced component.

Figure 14: Synchrotron microprobe XANES (a) and first derivative of XANES (b) for high-Fe points in 10 cm sample and hematite standard. These results indicate that the high-Fe points analyzed in this sample all contain hematite; no Fe-rich clays were detected.

Table 1. Bulk compositions in weight percent of basalt, saprolite and paleosol samples (Baker 2017), and calculated mafic index of alteration for both reducing (MIA-R) and oxidizing (MIA-O) conditions (Babechuk et al. 2014). All values are in wt % unless noted. LOI = loss on ignition. Bas = parent basalt. P = paleosol.

Sample	SiO_2	Al_2O_3	Fe_2O_3	MgO	CaO	Na_2O	K_2O	TiO_2	P_2O_5	MnO	LOI	C	Sum	Zr (ppm)	MIA-O	MIA-R
P	59.22	5.19	18.96	0.95	1.11	0.02	0.03	0.34	0.05	0.75	13.2	0.42	99.95	34	79	24
10 cm	46.60	13.58	15.47	1.94	2.92	0.71	0.08	0.53	0.03	0.02	18.0	0.4	99.95	68	67	39
15 cm	45.75	13.76	16.43	1.77	3.03	0.84	0.08	0.49	0.05	0.03	17.7	0.5	99.95	64	68	39
20 cm	48.13	21.67	3.33	1.46	5.70	2.62	0.31	5.02	1.15	0.06	10.2	0.17	99.82	319	56	51
30 cm	46.54	18.80	9.31	0.92	6.39	3.14	0.35	4.39	1.02	0.17	8.7	0.16	99.87	278	56	43
60 cm	46.66	19.32	8.71	0.92	6.29	3.08	0.34	4.51	1.05	0.13	8.7	0.06	99.87	282	56	44
80 cm	46.21	17.54	11.20	1.01	6.40	3.00	0.33	4.09	0.96	0.18	8.8	0.08	99.89	250	56	40
Bas	50.93	13.64	12.93	3.38	8.60	2.92	1.31	3.12	0.66	0.18	2.0	-	99.85	193	42	26

Table 2. Mobility ratios calculated on a volatile-free basis with respect to Zr from the data in Table 1.

	SiO_2	Al_2O_3	Fe_2O_3	MgO	CaO	Na_2O	K_2O	TiO_2	P_2O_5	MnO
T 0 P	5.600	1.160	7.324	0.595	-0.267	-0.961	-0.870	-0.381	-0.570	22.652
T 10 cm	1.597	1.826	2.396	0.629	-0.036	-0.310	-0.827	-0.518	-0.871	-0.685
T 15 cm	1.709	2.042	2.832	0.579	0.062	-0.132	-0.816	-0.526	-0.772	-0.497
T 20 cm	-0.428	-0.039	-0.844	-0.739	-0.599	-0.457	-0.857	-0.027	0.054	-0.798
T 30 cm	-0.366	-0.043	-0.500	-0.811	-0.484	-0.253	-0.815	-0.023	0.073	-0.344
T 60 cm	-0.373	-0.031	-0.539	-0.814	-0.499	-0.278	-0.822	-0.011	0.089	-0.506
T 80 cm	-0.300	-0.007	-0.331	-0.769	-0.425	-0.207	-0.806	0.012	0.123	-0.228

Figure 1

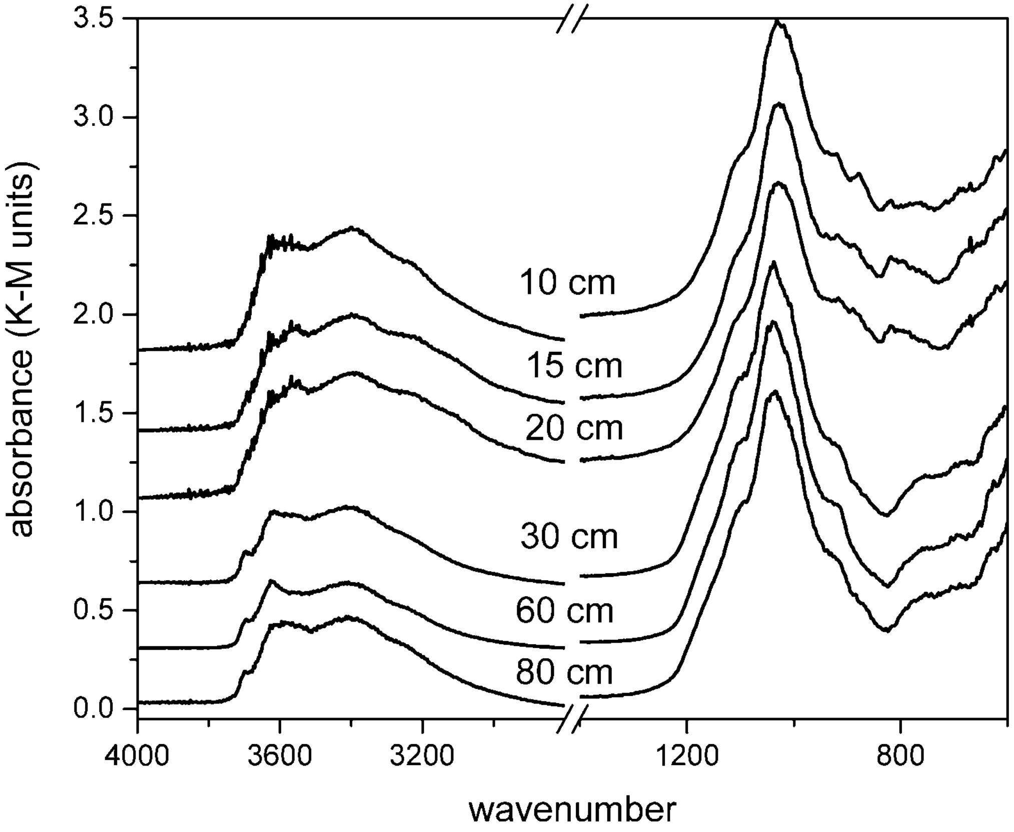
absorbance (K-M units)
0.0
0.5
1.0
1.5
2.0
2.5
3.0
3.5
4000
3600
3200
1200
800
wavenumber
10 cm
15 cm
20 cm
30 cm
60 cm
80 cm

Figure 2

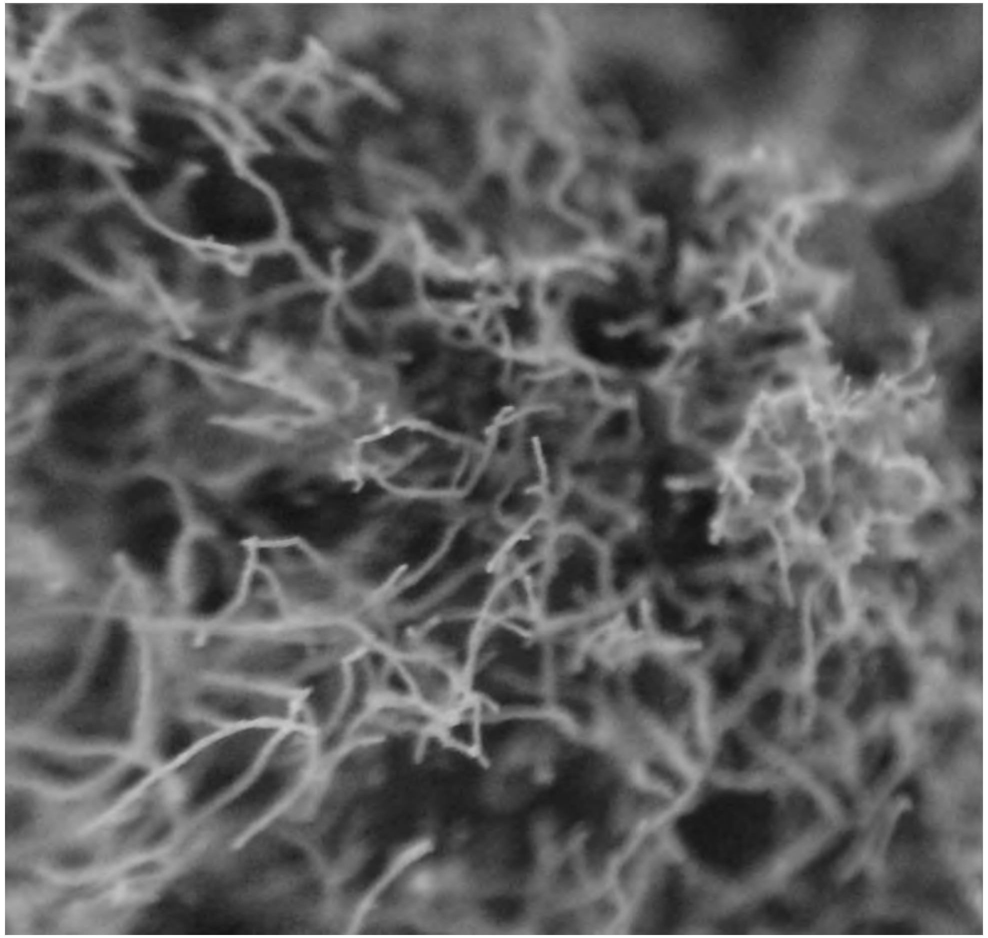

Figure 3

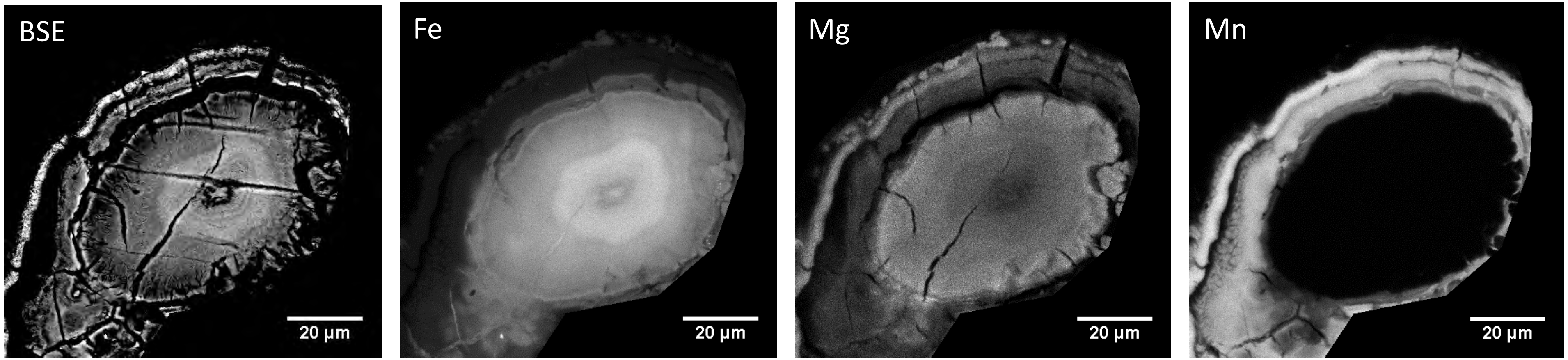

Figure 4

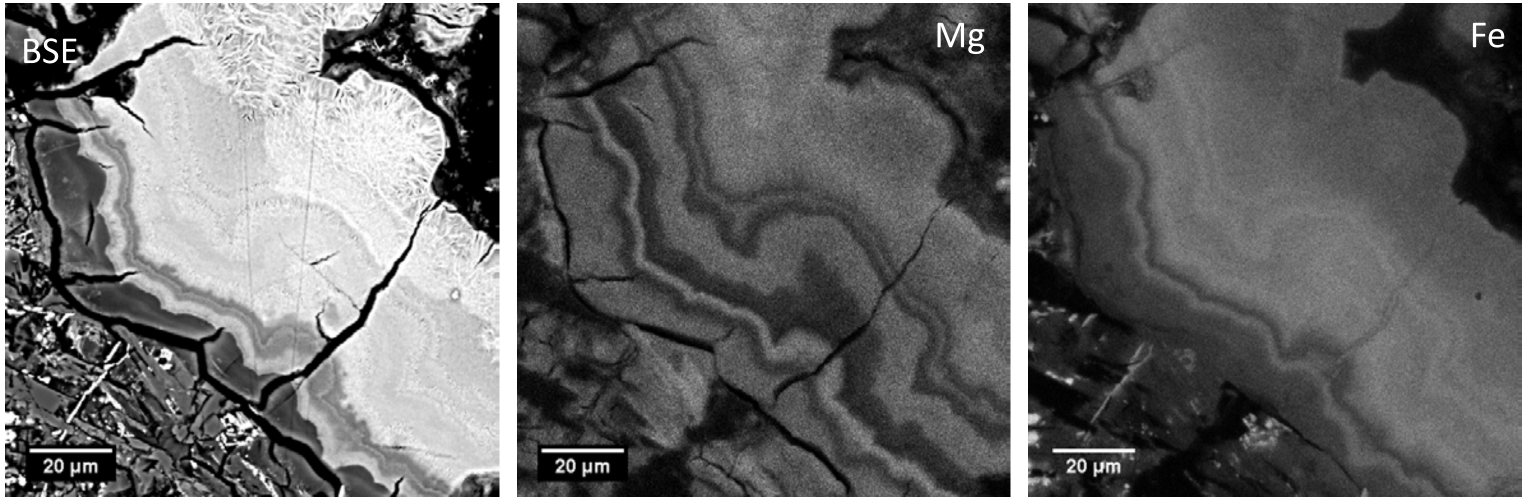

Figure 5

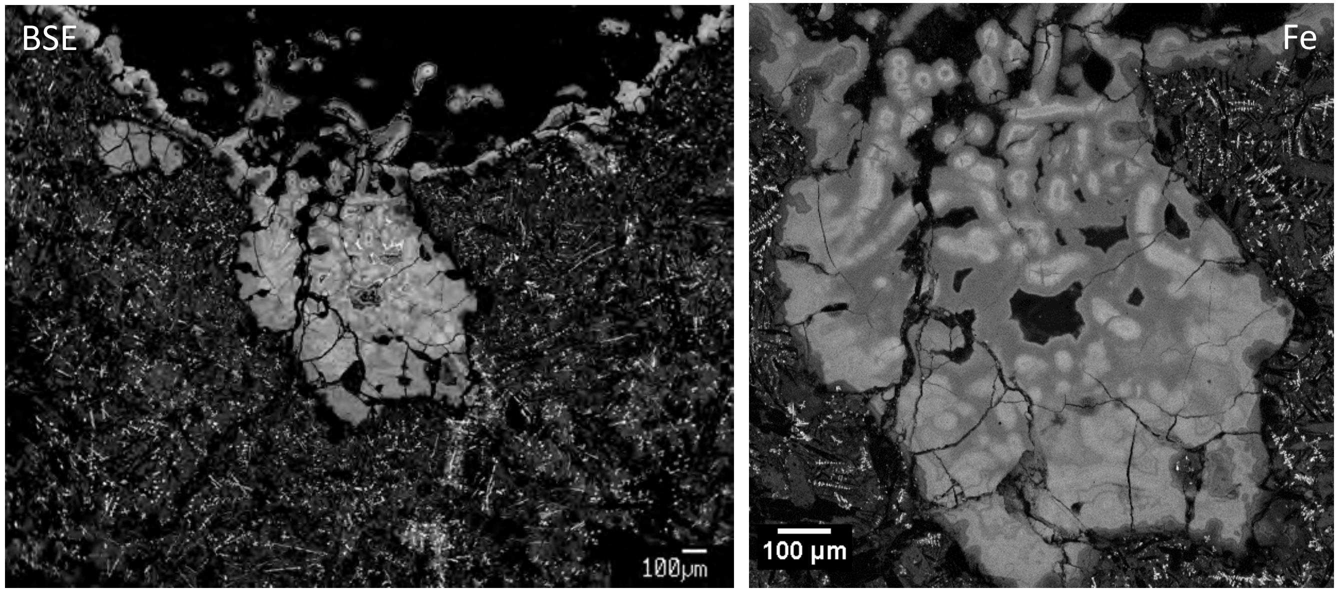

Figure 6

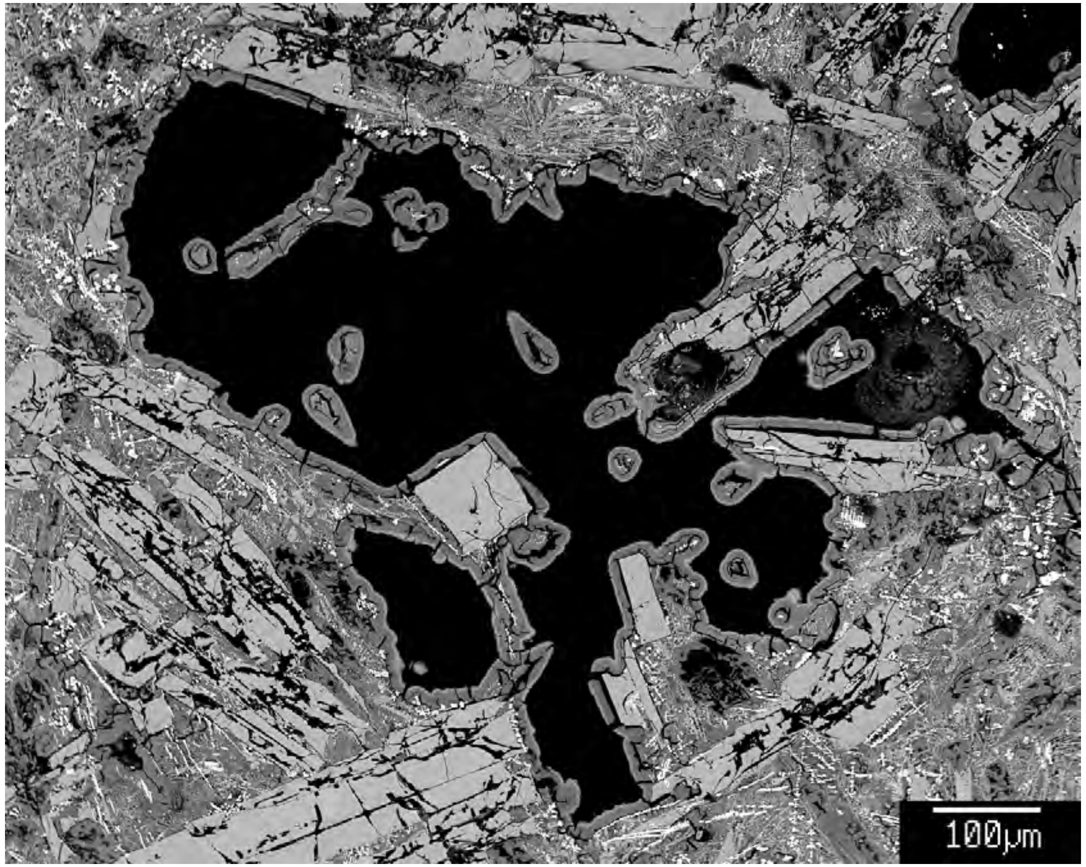

Figure 7

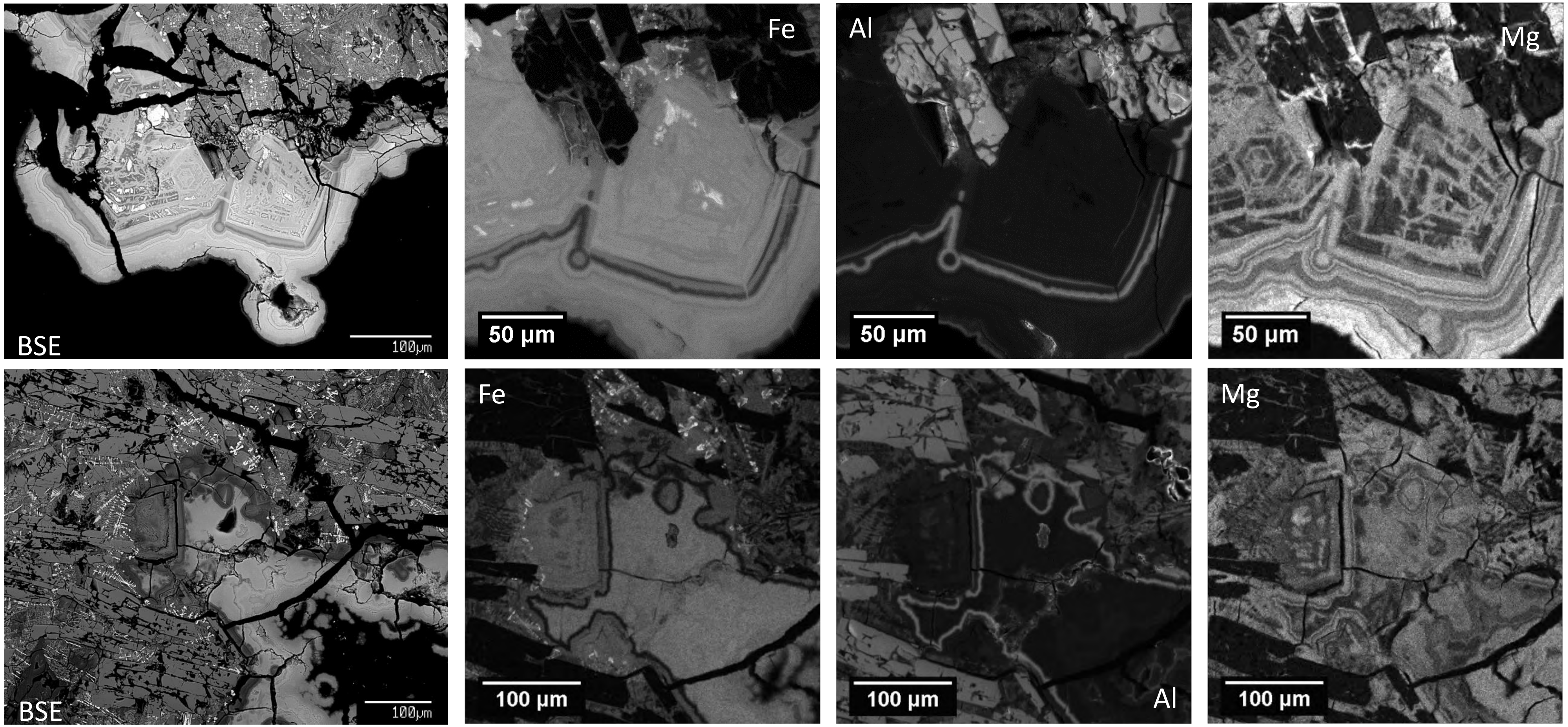
BSE
100µm
Fe
50 µm
Al
50 µm
Mg
50 µm
BSE
100µm
Fe
100 µm
100 µm
Al
Mg
100 µm

Figure 8

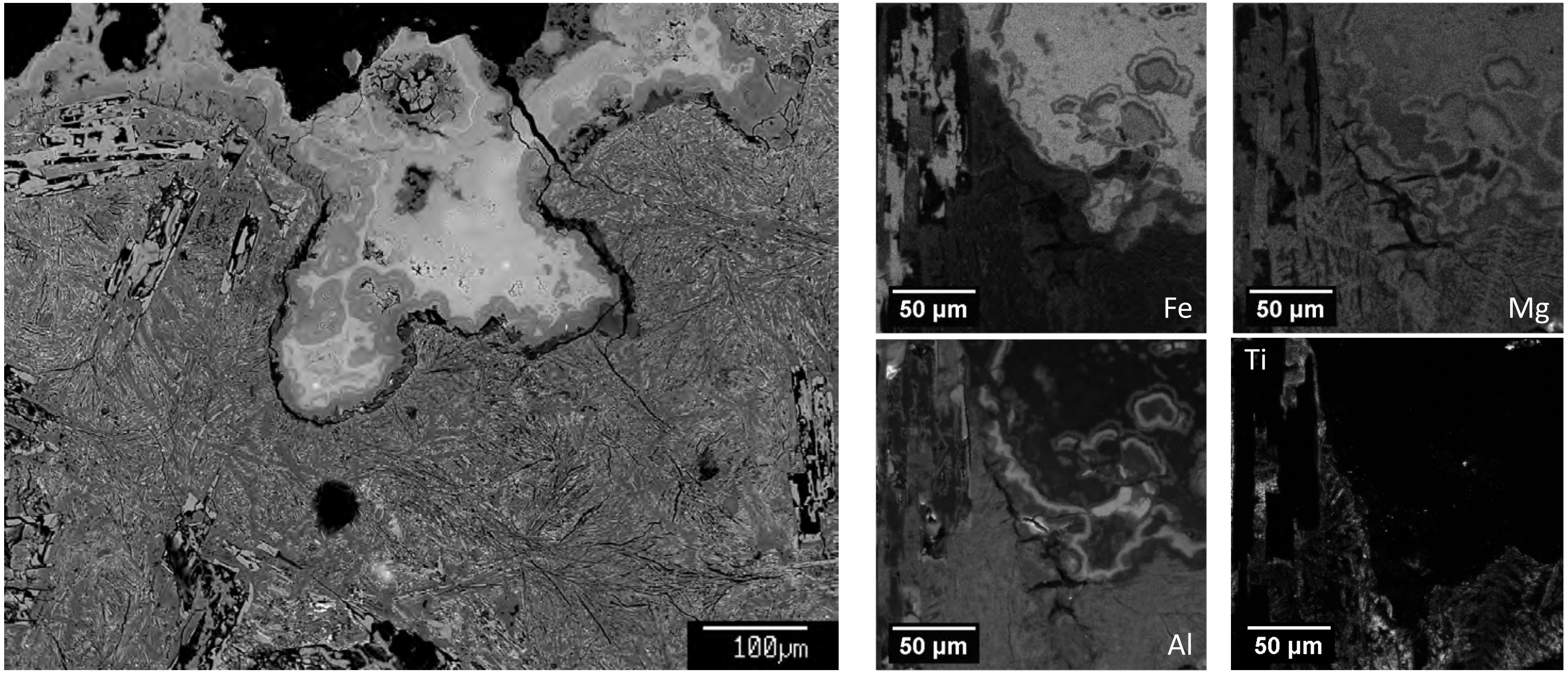

Figure 9

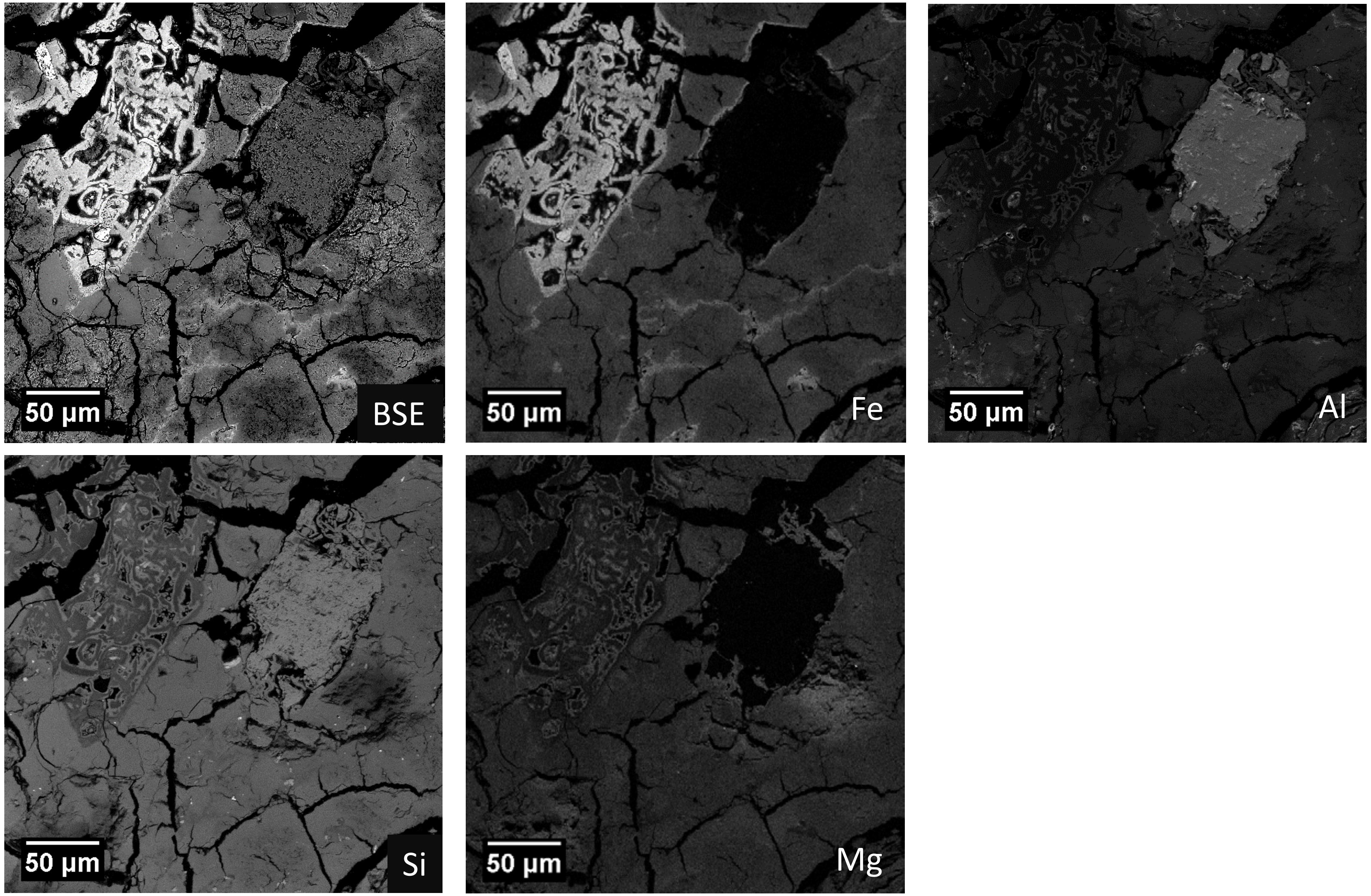

Figure 10

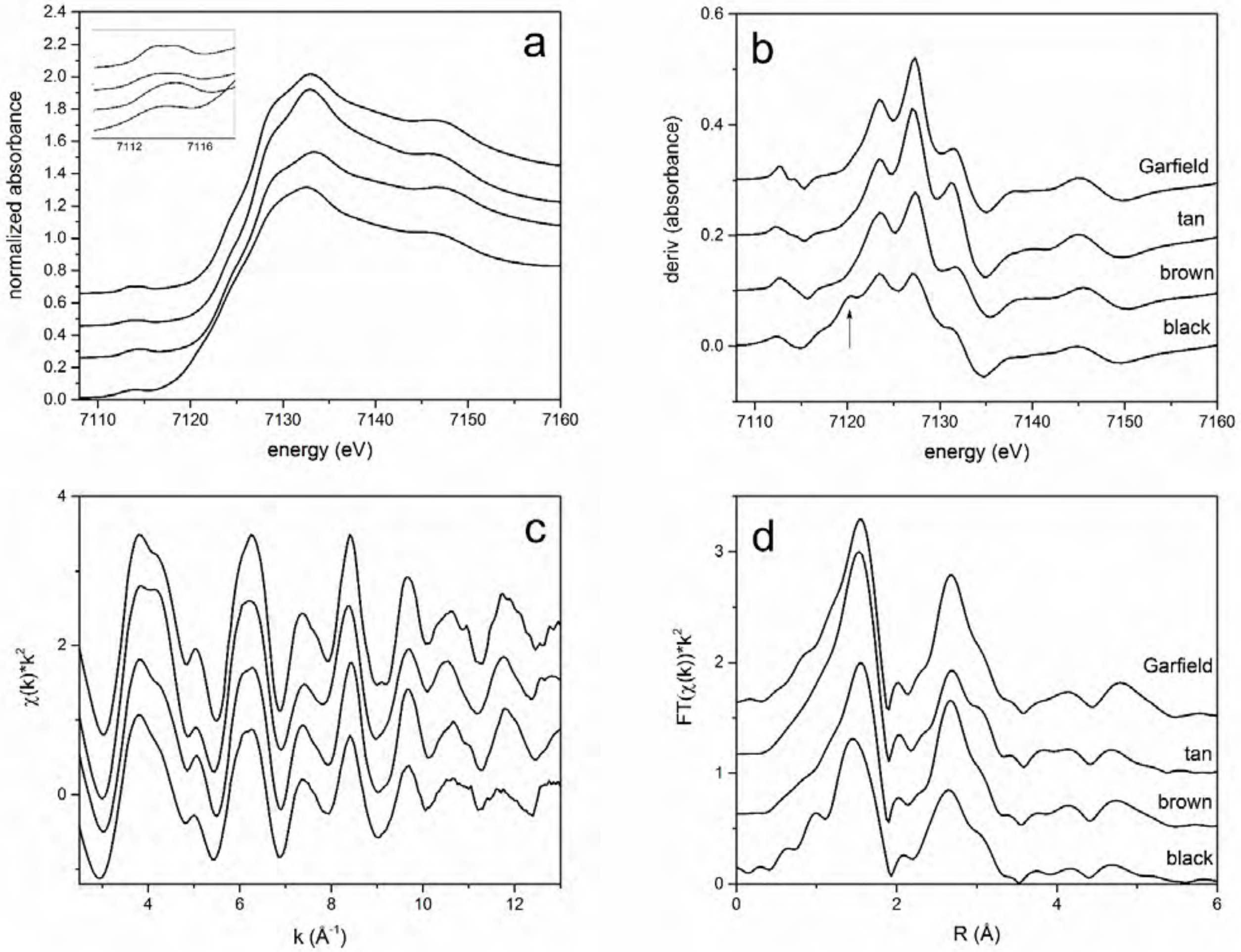
a
b
c
d
normalized absorbance
energy (eV)
7112
7116
deriv (absorbance)
Garfield
tan
brown
black
$\chi(k)*k^2$
k ($Å^{-1}$)
FT(χ(k))*k^2
R (Å)

Figure 11

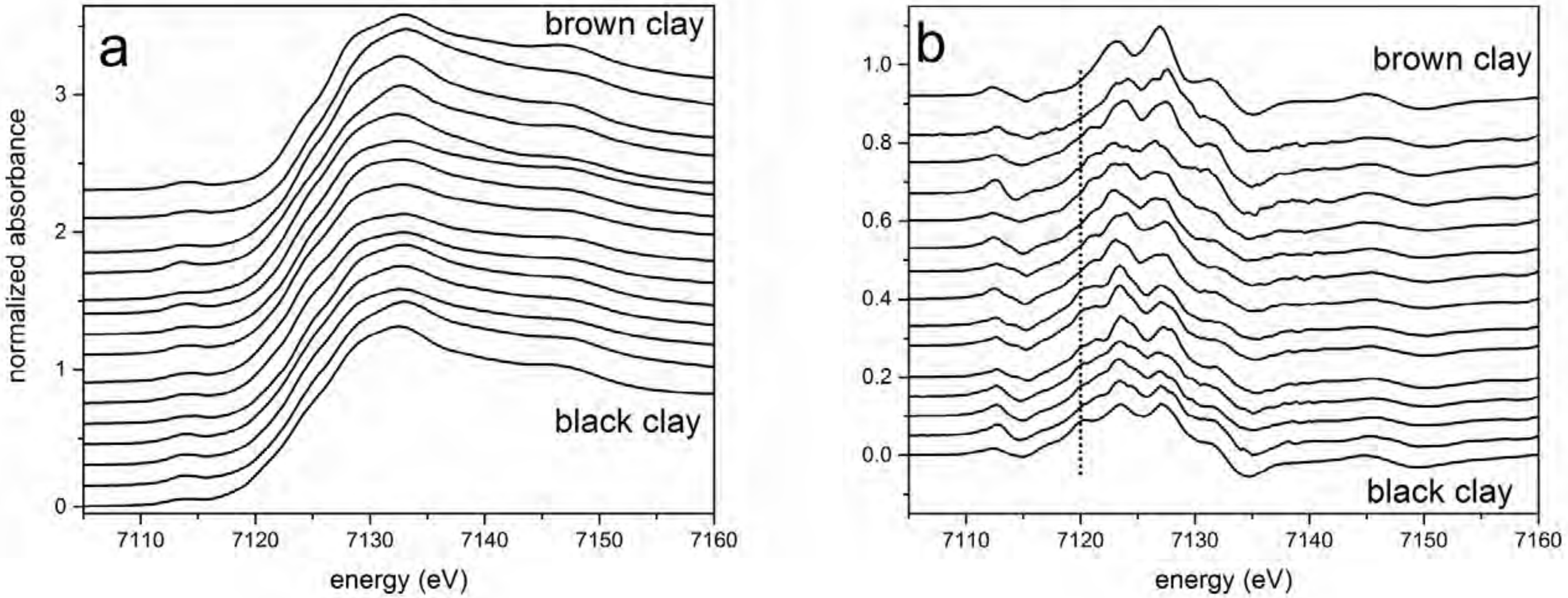
a
brown clay
black clay
normalized absorbance
0
1
2
3
7110
7120
7130
7140
7150
7160
energy (eV)
b
brown clay
black clay
0.0
0.2
0.4
0.6
0.8
1.0
7110
7120
7130
7140
7150
7160
energy (eV)

Figure 12

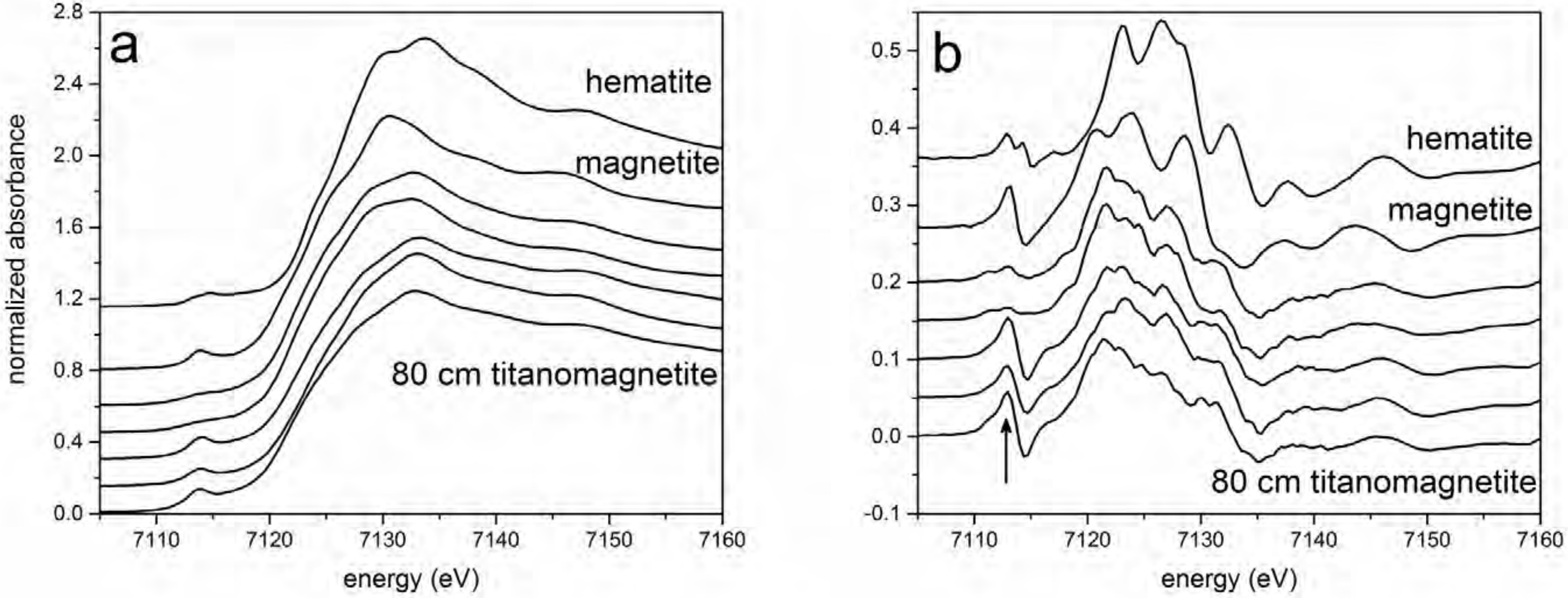
a
normalized absorbance
2.8
2.4
2.0
1.6
1.2
0.8
0.4
0.0
hematite
magnetite
80 cm titanomagnetite
7110
7120
7130
7140
7150
7160
energy (eV)
b
0.5
0.4
0.3
0.2
0.1
0.0
-0.1
hematite
magnetite
80 cm titanomagnetite
7110
7120
7130
7140
7150
7160
energy (eV)

Figure 13

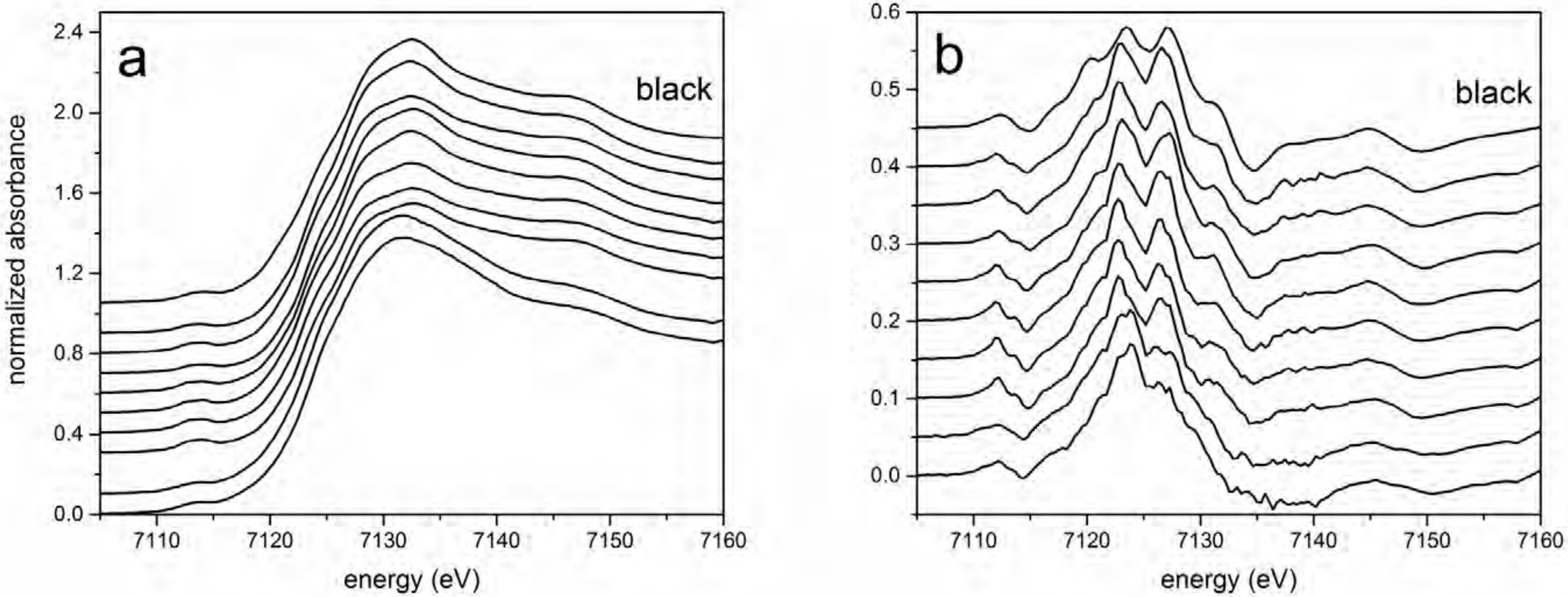
a
black
normalized absorbance
2.4
2.0
1.6
1.2
0.8
0.4
0.0
7110
7120
7130
7140
7150
7160
energy (eV)
b
black
0.6
0.5
0.4
0.3
0.2
0.1
0.0
7110
7120
7130
7140
7150
7160
energy (eV)

Figure 14

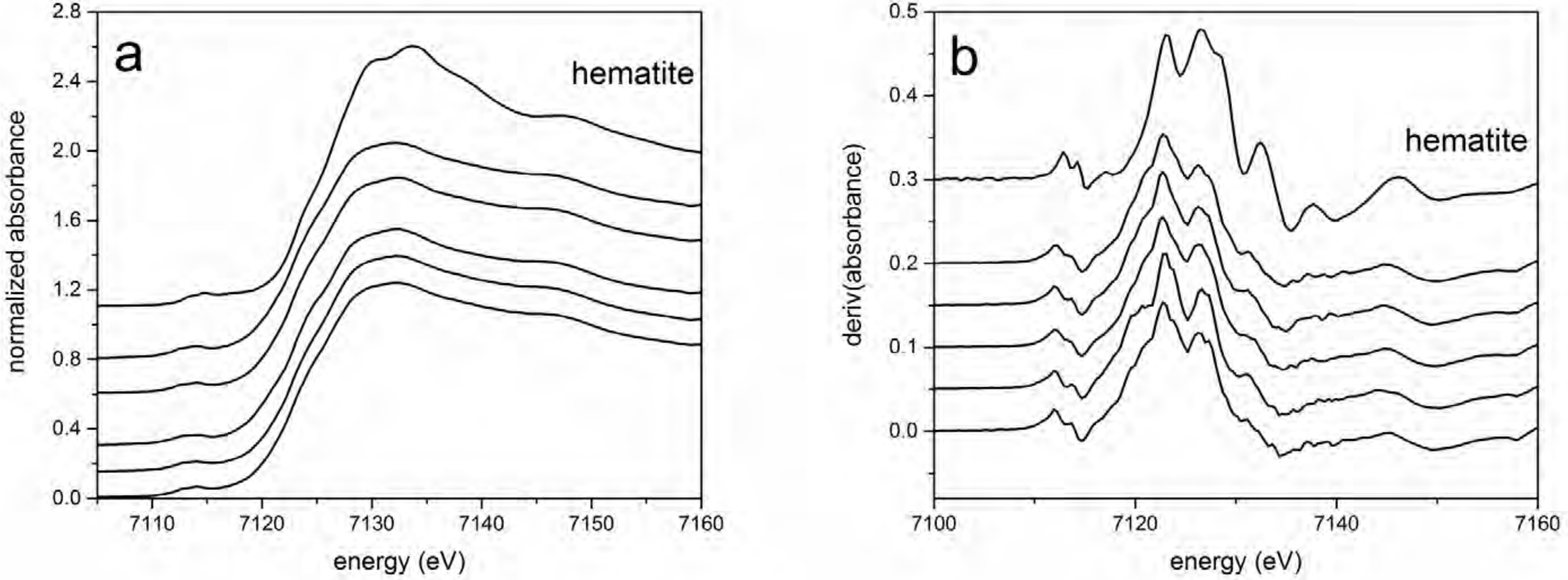
a
hematite
normalized absorbance
0.0
0.4
0.8
1.2
1.6
2.0
2.4
2.8
7110
7120
7130
7140
7150
7160
energy (eV)
b
hematite
deriv(absorbance)
0.0
0.1
0.2
0.3
0.4
0.5
7100
7120
7140
7160
energy (eV)